The Segmented Zambezi Sedimentary System from Source to Sink: 2. Geochemistry, Clay Minerals, and Detrital Geochronology

Eduardo Garzanti,[1,*] Germain Bayon,[2] Pedro Dinis,[3] Pieter Vermeesch,[4] Guido Pastore,[1] Alberto Resentini,[1] Marta Barbarano,[1] Lindani Ncube,[5] and Helena Johanna Van Niekerk[5]

1. Laboratory for Provenance Studies, Department of Earth and Environmental Sciences, University of Milano-Bicocca, 20126 Milan, Italy; 2. Unité de Recherche Geosciences Marines, IFREMER (Institut Français de Recherche pour l'Exploitation de la Mer), CS 10070, 29280 Plouzané, France; 3. University of Coimbra, MARE (Marine and Environmental Sciences Centre), Department of Earth Sciences, 3030-790 Coimbra, Portugal; 4. London Geochronology Centre, Department of Earth Sciences, University College London, London, WC1E 6BT, United Kingdom; 5. Department of Environmental Sciences, University of South Africa, Pretoria, South Africa

ABSTRACT

Elemental geochemistry, Nd isotopes, clay minerals, and U-Pb zircon ages integrated by petrographic and heavy-mineral data offer a multiproxy panorama of mud and sand composition across the Zambezi sediment-routing system. Detrital zircon geochronology highlights the four major episodes of crustal growth in southern Africa: Irumide ages predominate over Pan-African, Eburnean, and Neoarchean ages. Smectite, dominant in mud generated from Karoo basalts or in the equatorial/winter-dry climate of the Mozambican lowlands, prevails over illite and kaolinite. Elemental geochemistry reflects quartz addition by recycling (Uppermost Zambezi), supply from Karoo basalts (Upper Zambezi), and first-cycle provenance from Precambrian basements (Lower Zambezi). Mildly negative for sediments derived from mafic granulites, gabbros, and basalts, ε_{Nd} values are most negative for sand derived from cratonic gneisses. Intrasample variability among cohesive mud, very coarse silt, and sand is principally caused by the concentration of Nd-rich monazite in the fine tail of the size distribution. The settling-equivalence effect also explains deviations from the theoretical relationship between ε_{Nd} and $T_{Nd,DM}$ model ages, suggesting that monazite carries a more negative ε_{Nd} signal than less dense and less durable heavy minerals. Elemental geochemistry and Nd isotopes reveal that the Mazowe-Luenha river system contributes most of the sediment reaching the Zambezi delta today, with minor supply from the Shire River. Sediment yields and erosion rates are much lower on the low-relief Kalahari Plateau than in rugged Precambrian terranes. On the plateau, mineralogical and geochemical indices testify to extensive breakdown of feldspars and garnet unjustified by the present dry climate. Detrital kaolinite is recycled by incision of Cretaceous–Cenozoic paleosols even in the wetter lower catchment, where inefficient hydrolysis is testified to by abundant fresh feldspars and undepleted Ca and Na. Mud geochemistry and surficial corrosion of ferromagnesian minerals indicate that, at present, weathering increases only slightly downstream the Zambezi River.

Online enhancements: supplementary tables, data set, Google Earth map.

Introduction

The man who drinks Zambezi waters must always return to drink again. (Old Matabele saying, quoted in *The Leopard Hunts in Darkness*, by Wilbur Smith)

The Zambezi, the fourth-longest river in Africa and the largest draining into the Indian Ocean (fig. 1; Moore et al. 2007), underwent a still incompletely understood multistep evolution through time, influenced by rifting events that punctuated the ~280-Ma-long breakup history of Gondwana (Key et al. 2015). For large tracts the river flows along Permian–Triassic rift troughs, and its general eastward slope originated from domal uplift associated

Figure 1. The Zambezi drainage basin (base map from Google Earth). White circles indicate sampling locations (more information in a Google Earth file, available online). VF = Victoria Falls.

with the Early Cretaceous rifting of the South Atlantic in the west (Cox 1989; Moore and Blenkinsop 2002).

The modern drainage developed through the Neogene as a consequence of surface uplift of the broad Kalahari Plateau and southwestward propagation of the East African Rift, which created the tectonic depressions occupied by Lake Malawi in the east and the Okavango inland delta in the west (Ebinger and Scholz 2012). After diverse events of river capture and drainage reversal, a youthful lower course in Mozambique eroded backward to eventually connect with the upper course on the Kalahari Plateau, forcing it to plunge into Victoria Falls and the basaltic gorges downstream (Wellington 1955; Moore and Larkin 2001). The drainage basin continued to expand in the Quaternary, with the capture of the Angolan Kwando tributary and the currently incipient capture of the large Okavango River as well (Gumbricht et al. 2001).

In the Anthropocene, the course of the Zambezi ceased to be natural and was rigidly segmented by the construction of the great dams that created Lake Kariba (1958) and Lake Cahora Bassa (1974). Because the sediment-routing system (Hinderer 2012; Allen 2017) is strictly partitioned by these two major reservoirs, it is here convenient to distinguish four reaches: the Uppermost Zambezi headwaters as far as the Kwando confluence; the Upper Zambezi, which includes Victoria Falls and the gorges as far as Lake Kariba; the Middle Zambezi between the two reservoirs; and the Lower Zambezi downstream of Lake Cahora Bassa (fig. 1).

This study integrates the petrographic and heavy-mineral data illustrated and discussed in the companion paper (Garzanti et al. 2021*b*) with new data on elemental geochemistry, Nd isotope geochemistry, clay mineralogy, and detrital zircon geochronology from the same sample set. The two articles, in combination, provide a multiproxy characterization of sediment composition in the diverse tracts of the large Zambezi catchment, from the Zambian headwaters to the Mozambican coast. Our main aims are to (1) refine provenance diagnoses based on diverse compositional parameters from both mud and sand fractions of the sediment flux; (2) unravel the relative effects of source-rock lithology, recycling, hydraulic sorting, and chemical weathering on the mineralogical and chemical composition of mud and sand generated in humid subequatorial to

dry tropical climates; (3) infer sediment yields and erosion patterns in diverse parts of the large basin; and (4) evaluate the relative importance of chemical weathering as it occurs in present climatic conditions versus the mineralogical and chemical signatures of weathering inherited from past climatic conditions via recycling of detrital components.

Geology

The Zimbabwe Craton represents the northern part of Archean southern Africa (fig. 2A). A central terrane flanked by two distinct greenstone belts includes gneisses nonconformably overlain by volcanic rocks and conglomerates. The craton was stabilized between 2.7 and 2.6 Ga and eventually sealed by the Great Dike Swarm at 2575 Ma (Kusky 1998; Jelsma and Dirks 2002; Söderlund et al. 2010).

Tectonic activity continued through the Paleoproterozoic, when the proto–Kalahari Craton formed during the major Orosirian episode of crustal growth, and into the Mesoproterozoic, at the end of which the Kalahari Craton was eventually assembled (Hanson et al. 2006; Jacobs et al. 2008). Orosirian orogens include the Ubendian-Usagaran Belts along the southern margin of the Tanzania Craton and the Magondi Belt, exposing arc-related volcanosedimentary and plutonic rocks metamorphosed at amphibolite facies along the northwestern margin of the Zimbabwe Craton (Majaule et al. 2001; Master et al. 2010). The Angola Block, far to the west, represents instead the southern part of the Congo Craton. It comprises a central zone in the east, a central Eburnean zone, and the Lubango zone extending southward into Namibia, which recorded several distinct magmatic events between 2.0 and 1.77 Ga (De Carvalho et al. 2000; McCourt et al. 2013; Jelsma et al. 2018).

The next major episode of crustal growth is documented by the Irumide Belt extending from southern Zambia to Malawi. The external nappes exposed to the north of the Luangwa Rift include a 2.0–1.9 Ga gneissic basement overlain by quartzite, schist, and minor carbonate deposited around 1.85 Ga (Muva Supergroup). Granitoid suites were emplaced at 1.65–1.52, 1.36–1.33, and 1.05–0.95 Ga (De Waele et al. 2003). Regional metamorphism, increasing southeastward from greenschist facies to upper amphibolite facies, took place at 1.05–1.02 Ga (De Waele et al. 2006, 2009). The high-grade internal zone is exposed to the north of the lower Zambezi Valley between the Luangwa and Shire Rivers (southern Irumide Province; Alessio et al. 2019) and includes the Tete gabbro-anorthosite complex (~1.05 Ga; Westerhof et al. 2008). The

Choma-Kalomo Block, in southwestern Zambia, consists of crystalline basement covered by amphibolite facies paragneiss and schist yielding zircon grains of Paleoproterozoic age, intruded by two generations of Mesoproterozoic granitoid plutons (1.37 and 1.18 Ga; Bulambo et al. 2006) and documenting a thermal event between 1.02 and 0.98 Ma (Glynn et al. 2017).

The Kalahari Craton of southern Africa was eventually welded to the Congo Craton during the major Neoproterozoic Pan-African orogeny, testified to by the Damara-Lufilian-Zambezi Belt stretching from coastal Namibia to Mozambique (Frimmel et al. 2011; Fritz et al. 2013; Goscombe et al. 2020). The Lufilian Arc consists of Neoproterozoic metasedimentary and metaigneous rocks hosting Cu-Co-U and Pb-Zn mineralizations (Kampunzu and Cailteux 1999; John et al. 2004; Eglinger et al. 2016). The Zambezi Belt contains a volcanosedimentary succession deformed under amphibolite facies conditions at 0.9–0.8 Ga (Hanson 2003), whereas eclogite facies metamorphism dated at 592 Ma constrains the timing of subduction and basin closure (John et al. 2003), with thrust emplacement dated as 550–530 Ma (Hargrove et al. 2003).

The Gondwana supercontinent, assembled during the Pan-African orogeny, started to be disrupted toward the close of the Paleozoic, when Karoo sediments began to accumulate in several depocenters across southern Africa. Karoo basins include the elongated Gwembe and Luangwa troughs that control the drainage of the Middle Zambezi and Luangwa Rivers, respectively (Nugent 1990). The severalkilometer-thick Karoo Supergroup begins with upper Carboniferous to lowermost Permian diamictite, followed by Permian to Middle Triassic turbidite and coal-bearing fluviodeltaic strata. Permian sandstones contain andesitic-dacitic volcanic detritus (Johnson 1991) and interlayered tuffs yielding ages mainly between 270 and 260 Ma (Lanci et al. 2013; McKay et al. 2016). Subsidence in the southern retroarc basin was associated with subduction of paleo-Pacific lithosphere, while transtensional stress propagated southward from the Neotethyan rift in the north (Catuneanu et al. 2005). The upper part of the succession consists of Upper Triassic to Lower Jurassic braidplain sandstones, floodplain mudrocks, and aeolian sandstones (Johnson et al. 1996). Karoo sedimentation was terminated by flood-basalt eruptions recorded throughout southern Africa around 183 Ma (Svensen et al. 2012; Greber et al. 2020).

In the Early Cretaceous, opening of the Indian Ocean led to formation of sedimentary basins and extensive volcanism in the Mozambique Channel. In the Cenozoic, fluvial and lacustrine sediments,
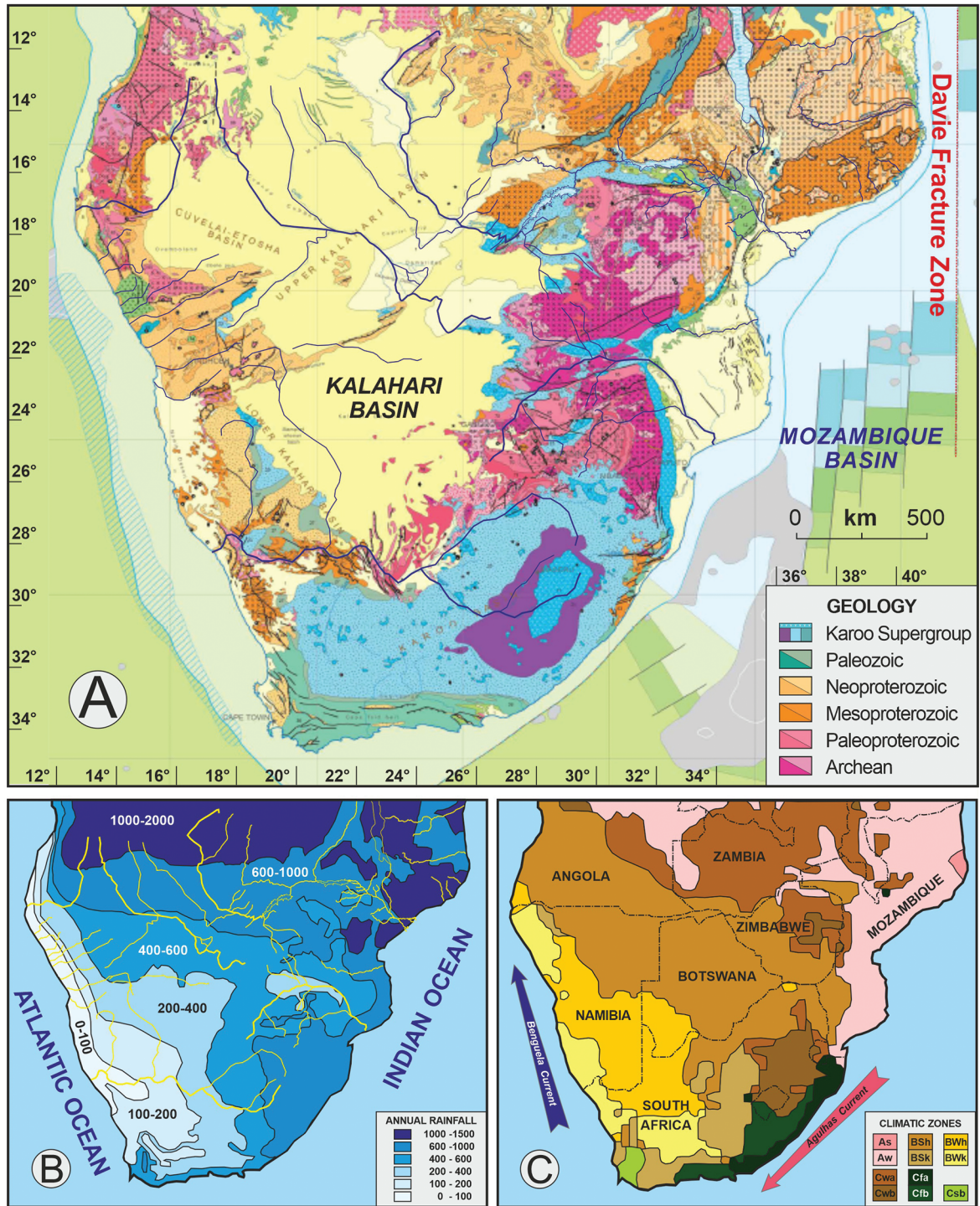
Figure 2. Geology and climate of southern Africa. *A*, Geological map (Thiéblemont et al. 2016). *B*, Precipitation gradients (in mm): east–west, from warm Indian Ocean to cool Atlantic Ocean; south–north, from Kalahari dryland to humid Congo. *C*, Distribution of climatic zones (Köppen-Geiger classification; Kottek et al. 2006): A = equatorial, B = arid, C = warm temperate. Precipitation: W = desert, S = steppe, f = fully humid, s = summer dry, w = winter dry. Temperature: h = hot arid, k = cold arid, a = hot summer, and b = warm summer.

including basal gravel and sand with calcrete, were deposited inland in the Kalahari Basin, hosting the largest continuous sand sea on Earth, where repeated phases of eolian deposition took place through the Quaternary (Haddon and McCarthy 2005; Burrough et al. 2019). Southwestward propagation of the East African rift in the late Neogene (Daly et al. 2020) eventually reached the Kalahari region, where fault-related subsidence in the Okavango Rift is exerting a major control on drainage patterns (McCarthy et al. 2002; Vainer et al. 2021).

Geomorphology and River Drainage

Climate. Southern Africa, with its largely rural population dependent on rain-fed subsistence agriculture, is particularly vulnerable to climate variability and extreme events. These include severe droughts affecting much of Zambia, Malawi, Zimbabwe, or northern South Africa, alternating with devastating floods such as those periodically striking Mozambique. Cyclones occur in the wet season, and in 2019 two cyclones caused floods and destruction in the same year for the first time (Siwedza et al. 2021). Climate variability has a multitude of forcing factors that interact with each other and wax and wane in their importance through time (Reason et al. 2006; Howard and Washington 2019). Overall, rainfall increases from west to east at subtropical latitudes and from south to north at subequatorial latitudes, the principal sources of humidity being the Indian Ocean in the east and the Atlantic Ocean in the northwest (fig. 2B).

The African continent divides the tropical high-pressure zone into the Indian Ocean and South Atlantic anticyclones, particularly during the austral summer, when heating of the landmass reaches its maximum. Moisture derived primarily from air masses moving inland from the warm Indian Ocean is reduced by orographic effects along the eastern escarpment and declines progressively westward, resulting in increasing aridity. Descending, divergent air masses occur throughout the year along the west coast, where the temperature inversion is reinforced by the northward-flowing Benguela current and upwelling of cold Antarctic waters offshore. Dominant southwesterly winds are dry and thus contribute to the marked westward decrease in rainfall across the subcontinent. A sharp contrast thus exists between humid coastal Mozambique (maximum annual rainfall of 1.5 m) and the Kalahari Plateau inland, where quasistationary anticyclonic conditions prevail (fig. 2C). Mozambique is characterized by a tropical climate, with a wet season from October to March and a dry season from April to September (average annual rainfall of ~0.65 m at Tete).

In subequatorial southern Africa, atmospheric circulation is complex. Moist South Atlantic air moved inland by westerly winds converges with Indian Ocean air along the Congo Air Boundary, frequently associated with development of pressure lows and widespread rains across the Kalahari Plateau. Annual rainfall, chiefly associated with the southward shift of the Intertropical Convergence Zone, reaches 1.4 m in Angola during summer (Jury 2010). In winter, when the Intertropical Convergence Zone and the Congo Air Boundary migrate northward, interior southern Africa remains generally dry under the influence of the Indian Ocean anticyclone.

The River System. The Zambezi (length: 2575 km, basin area: $\sim 1.4 \times 10^6$ km^2) is the largest river of southern Africa. Sourced in northwesternmost Zambia among low ridges of the Kasai Shield (part of the Congo Craton), the river traverses unconsolidated Kalahari sands in the Barotse floodplain, a 30–50-km-wide wetland flooded for several months by Zambezi waters after the rainy season (peak discharge in April).

The Uppermost Zambezi starts to flow more swiftly as it first encounters basaltic bedrock at Ngonye Falls, and it is next joined by the Kwando River, draining the Kalahari Basin in humid Angola. While entering the Okavango Rift, the Kwando (here named Linyanti and next Chobe) deviates sharply eastward along a tectonic depression hosting large swamps and once-large paleolakes (Burrough et al. 2009; Moore et al. 2012). The graben continues eastward into the Machili Flats, drained by the low-gradient Kasaya and Ngwezi Rivers, eastern Zambezi tributaries sourced in the Lufilian arc and the Choma-Kalomo Block, respectively.

Downstream of the Kwando confluence, the Upper Zambezi and its local tributaries—including the Sinde River, sourced in the Choma-Kalomo Block—incise into Karoo basaltic lavas, and the gradient steepens, forming minor rapids upstream of Victoria Falls. Next, after plunging some 100 m into the falls, turbulent Upper Zambezi waters design an astonishing zigzag into steep gorges of black basalt, the result of progressive retreat of the waterfalls during the Quaternary (Derricourt 1976). After receiving tributaries draining Karoo lavas overlain by thin Kalahari dune sand (e.g., Masuie and Matetsi), the Zambezi reaches Lake Kariba shortly downstream of the confluence with the Gwai River. Sourced in the Zimbabwe Craton, the low-gradient senile upper course of the Gwai River is incised—as are its east-bank tributaries Umguza and Shangani—

in Karoo basalt and sedimentary rocks surrounded by Kalahari dune sand (Thomas and Shaw 1988; Moore et al. 2009). In the youthful lower tract, the Gwai cuts steeply across the Dete-Kamativi Inlier of the Paleoproterozoic Magondi Belt (Glynn et al. 2020) and receives the eastern Tinde tributary, mainly draining Pan-African molasse (Goscombe et al. 2020).

The Middle Zambezi, between Lakes Kariba and Cahora Bassa, flows along a Karoo rift trough formed along the Pan-African (Kuunga) suture zone (Goscombe et al. 2020) and hosting a thick infill of basalt-capped Permian–Triassic sedimentary rocks overlying Ordovician–Devonian siliciclastic strata (Nyambe 1999). The major tributaries in this tract are the Kafue and the Luangwa, both from Zambia. The Kafue, the longest Zambezi tributary (length: 1576 km, basin area: 154,200 km^2), is sourced in the Lufilian arc, flows across a 240-km-long, swampy, flat floodplain, and next drops 550 m into a 60-km-long gorge carved in gneiss and metasedimentary rocks of the West Zambezi Belt to join the Zambezi ~75 km downstream of Lake Kariba. The Luangwa (length: 770 km, basin area: 151,400 km^2) is sourced in the Ubendian Belt and flows for most of its course along a Karoo rift trough filled with an 8-km-thick Permian–Triassic sedimentary succession (Banks et al. 1995), separating the external nappes of the Irumide Belt in the north from the high-grade southern Irumide Province in the south. After cutting across southern Irumide granulites, the Luangwa joins the Zambezi just upstream of Lake Cahora Bassa.

The Lower Zambezi in Mozambique receives tributaries from the west (Sangara, Mufa) and north (Luia, Morrunguze) that largely drain high-grade southern Irumide rocks. The largest tributary is the Shire (from *chiri* = steep banks), the outlet of Lake Malawi, which drains largely garnet-free mafic granulites of the Blantyre domain (southern Malawi-Unango Complex), where middle-lower crust at the southern margin of the Congo Craton underwent high-grade metamorphism at ~920 Ma (Goscombe et al. 2020). From the west, the Mazowe and Luenha Rivers drain well into the Archean Zimbabwe Craton in the headwaters. Downstream, the two rivers cut across the polymetamorphic Mudzi migmatitic gneisses remobilized during the Pan-African orogeny and next across the Neoproterozoic Marginal Gneiss. Lowermost-course tributaries include the Sangadze and Zangue Rivers, sourced in the Pan-African Um-kondo Belt, comprising greenschist facies to lower amphibolite facies schists thrust onto the margin of the Zimbabwe Craton and upper amphibolite facies to granulite facies gneisses in the core (Stenian Barue Complex). The northern Minjova tributary largely drains the Moatize-Minjova Basin filled by coal-bearing Permian–Triassic Karoo clastic rocks (Fernandes et al. 2015).

In the lowermost tract, the Zambezi River flows along the Lower Zambezi graben, originated as a failed arm of the Middle Jurassic Mozambique Basin rift (Butt and Gould 2018). Zambezi sediments have built through time the largest continental shelf along the Indian Ocean coast of Africa (Walford et al. 2005; Ponte et al. 2019). Large sediment volumes, however, are not deposited in front of the Zambezi mouth but dragged northeastward by longshore currents (Schulz et al. 2011; van der Lubbe et al. 2014), forming wide beaches as far as Quelimane and beyond (e.g., Praia da Madal; fig. 1).

The Zambezi in the Anthropocene. The course of the Zambezi has been profoundly modified by man since the second half of the twentieth century. The Kariba and Cahora Bassa Dams built on the main stem, as well as others built on major tributaries, have substantially altered the hydrological regime of the Zambezi River and its delta and have disrupted the natural sediment-routing system, efficiently trapping detritus generated upstream (Davies et al. 2000; Beilfuss and dos Santos 2001; Calamita et al. 2019). Lake Kariba (length: 223 km, storage capacity: 185 km^3) is the world's largest artificial reservoir, whereas Lake Cahora Bassa (length: 292 km, storage capacity: 73 km^3) is Africa's fourth-largest (Vörösmarty and Moore 1991).

Since Zambia's independence, two big dams have been built also on the Kafue River, at Itezhi-Tezhi ("slippery rock") and in the Kafue Gorge. The Itezhi-Tezhi Dam (storage capacity: 6 km^3, completed in 1977) closes the gap through a ridge of ~100-m-high hills where the paleo-Kafue—once flowing south-ward toward Lake Makgadikgadi and the Limpopo River—was captured and started to flow eastward as part of the Zambezi drainage (Thomas and Shaw 1991; Moore and Larkin 2001). Downstream, the river flows sluggishly in the maze of swampy channels and lagoons of the Kafue Flats and next plunges into the Kafue Gorge, where other dams have been constructed (Upper Kafue Gorge; storage capacity: 0.8 km^3, operational since 1973) or are under construction (Lower Kafue Gorge). Other dams were built (e.g., Nkhula, Tedzani, Kapichira), or are planned, on the Shire River in southern Malawi. Besides human intervention, the Zambezi sediment-routing system is segmented by natural processes as well, much sediment being retained in large wetlands such as the Barotse floodplain and Chobe swamps on the Uppermost Zambezi, the Kafue Flats, or the Elephant Marsh on the Shire River (Bolton 1984; Moore et al. 2007).

Sediment Fluxes. Information on sediment loads transported both before and after the construction of the big dams is largely missing throughout the Zambezi drainage basin. In the lack of accurately gauged sediment fluxes, estimates on annual solid transport range widely between 20 million and 100 million tons (Hay 1998), with a median value around 50 million tons (Milliman and Meade 1983; ERM 2011; Milliman and Farnsworth 2011). These figures correspond to an average annual sediment yield and erosion rate between 15 and 70 tons/km^2 and between 0.005 and 0.03 mm, respectively (median values: ~35 tons/km^2 and ~0.01 mm). On the basis of cosmogenic nuclide data, the annual Uppermost Zambezi sediment flux was estimated as 5.5 ± 0.6 million tons (Wittmann et al. 2020), corresponding to a sediment yield and erosion rate of 16 ± 2 tons/km^2 and 0.006 ± 0.001 mm. An annual sediment volume of only 100,000 m^3, ascribed to a low topographic gradient and the presence of vast wetlands on the Kalahari Plateau, was estimated at Victoria Falls, whereas nearly half of the sediment flux (22 million out of 51 million m^3) was considered as generated in the Lower Zambezi catchment (FFEM 2005; van der Lubbe et al. 2016). After closure of the Kariba and Cahora Bassa Dams, annual sediment supply to the Zambezi Delta may have been reduced to as low as 0.8 million m^3, between 1% and 7% of which is bedload (Ronco et al. 2010 p. 52; ERM 2011).

Uncertain by an order of magnitude are also the estimates of sediment accumulation in Lake Kariba (between 7 million and 70 million tons, according to Bolton 1984, but only ~4 million tons, according to Kunz et al. 2011) and Lake Cahora Bassa (between 20 million and 200 million tons, according to Bolton 1984, and 28.6 million m^3, according to Ronco et al. 2010, p. 47). From sparse data on sediment concentration, annual sediment yields of 40 and 200 tons/km^2 were estimated for the Gwai and Luangwa catchments, respectively, corresponding to average erosion rates of 0.015 and 0.075 mm (Bolton 1984). Similar values were evaluated for minor tributaries in Zambia and Mozambique (200 tons/km^2) and for the Luangwa and the rest of the Middle Zambezi (170–250 tons/km^2, from sediment volumes of 14.0 million and 14.6 million m^3, respectively; Ronco et al. 2010, p. 47). Very high annual rates of soil loss (up to 2900 tons/km^2) are reported from the Shire catchment in southern Malawi (Mzuza et al. 2019).

Methods

Between 2011 and 2019, 71 sediment samples were collected from active sand bars (57), levees (2), and freshly deposited muds (12) of the Zambezi River and its major tributaries, from the source in northwesternmost Zambia to the delta in Mozambique. Full information on sampling sites is provided in table A1 and a Google Earth file (tables A1–A7 and the Google Earth file are available online).

Clay and Silt Mineralogy. The mineralogy of six mud samples from the Middle and Lower Zambezi main stem and tributaries (Kafue, Sangadze, Shire) was determined on both <32-μm and <2-μm fractions by X-ray powder diffraction (XRD) using PANalytical Aeris equipment with a Cu tube, at 15 kV and 40 mA. The <32-μm fraction was separated by wet sieving, and diffractograms were performed on randomly oriented powder in the range 2°–60° (2θ). The <2-μm fraction, separated by centrifuging according to Stokes's law, was analyzed on oriented aggregates after air drying (2°–30° 2θ), solvation with ethylene glycol, and heating at 550°C (2°–15° 2θ). Mineral proportions were evaluated semiquantitatively using diagnostic XRD peak areas (Moore and Reynolds 1997; Kahle et al. 2002). Further technical information is provided in Dinis et al. (2020*b*). The XRD data previously obtained on the <32-μm fraction of mud samples collected from the Upper Zambezi catchment and main tributaries, including the Kwando and the Gwai (Garzanti et al. 2014*a*; Setti et al. 2014), were also considered. The mineralogical data set is provided in tables 1 and A2.

Mud and Sand Geochemistry. Chemical analyses of 51 sediment samples were carried out at Bureau Veritas Mineral Laboratories (Vancouver, Canada) on quartered aliquots of the <32-μm (18 river muds) and 63–2000-μm (31 river sands) fractions obtained by wet sieving. Two levee silty sands were analyzed in bulk. Following a lithium metaborate/tetraborate fusion and nitric acid digestion, major oxides and several minor elements were determined by ICP emission spectrometry and trace elements by ICP-MS (see app. A and http://acmelab.com for detailed information on adopted procedures, standards used, and precision for elements of group 4A–4B and codes LF200 and LF300; apps. A and B are available online).

Classic multielement chemical indices used to estimate weathering and calculated from molar proportions of mobile alkali and alkaline-earth metals include the WIP (weathering index of Parker 1970) and the CIA (chemical index of alteration; Nesbitt and Young 1982). The WIP, however, merely measures the amount of a set of mobile elements that decreases rapidly wherever quartz is added to the sediment, making it an index of quartz recycling more than an index of weathering. Because correcting the CIA for CaO in carbonates introduces uncertainties (Garzanti

Table 1. Silt and Clay Mineralogy in the Zambezi Catchment Determined by X-Ray Powder Diffraction

River	Bulk sample (<32-μm fraction, wet sieved)								Clay minerals (<2 μm)					
	Qz	KF	Pl	Carb	Amp	Hem	Phyll	Total	Sme	Ill	Chl	Kao	Total	Kao/(Ill + Chl)
Uppermost Zambezi	49	15	1	0	0	0	35	100.0	43	21	0	36	100.0	1.7
Ngwezi	33	11	6	0	0	0	50	100.0	76	6	0	18	100.0	3.0
Kwando	89	0	0	4	0	0	7	100.0	70	13	0	17	100.0	1.3
Sinde	14	6	17	0	0	10	53	100.0	87	0	0	13	100.0	∞
Zambezi at Victoria Falls	75	8	2	0	0	0	15	100.0	78	15	0	7	100.0	.5
Matetsi	7	20	15	4	0	9	45	100.0	93	0	0	7	100.0	∞
Upper Zambezi	41	12	15	0	0	5	27	100.0	54	31	0	15	100.0	.5
Upper Zambezi	43	11	19	0	0	4	23	100.0	50	33	0	17	100.0	.5
Umguza	26	8	7	3	0	0	56	100.0	87	4	5	4	100.0	.4
Upper Gwai	20	4	4	3	0	0	69	100.0	77	5	5	13	100.0	1.3
Tinde	34	24	5	0	0	0	37	100.0	25	40	9	26	100.0	.5
Kafue	9	7	11	2	2	1	69	100.0	27	54	.5	19	100.0	.3
Middle Zambezi	10	7	11	6	1	.2	64	100.0	60	27	0	12	100.0	.4
Zambezi at Tete	19	5	19	0	2	0	54	100.0	25	37	0	38	100.0	1.0
Sangadze	12	8	10	3	.1	0	67	100.0	96	3	0	1	100.0	.4
Shire	14	7	16	0	2	0	61	100.0	9	49	0	42	100.0	.9
Lower Zambezi	17	14	20	0	0	0	49	100.0	52	35	0	12	100.0	.4

Note. Qz = quartz; KF = K-feldspar; Pl = plagioclase; Carb = carbonate; Amp = amphibole; Hem = hematite; Phyll = phyllosilicate; Sme = smectite; Ill = mica/illite; Chl = chlorite (including vermiculite); Kao = kaolinite.

and Resentini 2016), in this study we use the CIA* corrected only for CaO in apatite (CIA* = 100 · $Al_2O_3/[Al_2O_3 + (CaO - 3.33 \times P_2O_5) + Na_2O + K_2O]$). The weathering effect is best detangled from other controls on geochemical composition if mobile elements (Mg, Ca, Na, K, Sr, and Ba) are considered one by one. This can be done by using $\alpha^{Al}E$ values, defined as $(Al/E)_{sample}/(Al/E)_{standard}$ (Garzanti et al. 2013a, 2013b), which compare the concentration of any mobile element E with reference to nonmobile Al in our samples to an appropriately selected standard composition (e.g., the UCC [upper continental crust] standard of Taylor and McLennan 1995; Rudnick and Gao 2003). Aluminium, hosted in a wide range of rock-forming minerals with diverse density, shape, and size, including phyllosilicates (concentrated in mud) and feldspars (concentrated in sand), is used as a reference for all elements rather than Ti, Nd, Sm, or Th (Gaillardet et al. 1999), which are hosted preferentially in ultradense minerals and thus may reach strongly anomalous concentrations as a result of hydrodynamic processes. Geochemical data are summarized in table 2 and provided in full in table A3.

Nd Isotope Geochemistry.   Sixteen samples from the Middle and Lower Zambezi catchments were treated with a sequential leaching procedure for quantitative removal of carbonates, Fe oxide phases, and organic matter (Bayon et al. 2002). Before geochemical analyses, about 80 mg of powdered samples were digested by a HF-HCl-HNO$_3$ mixture (seven <32-μm fractions, nine 32–63-μm classes, and two bulk samples) or alkaline fusion (14 63–2000-μm fractions). Selected major- and trace-element abundances were determined at the Pôle Spectrométrie Océan (PSO) with a Thermo Scientific Element XR sector field ICP-MS, using the Tm addition method (Barrat et al. 1996). Both the accuracy and the precision of measured concentrations were assessed by analyzing three certified reference materials (AN-G, AGV-1, BCR-1).

Neodymium isotopes were measured at PSO with a Thermo Scientific Neptune multicollector ICP-MS, after Nd purification by conventional ion chromatography. Repeated analyses of a JNdi-1 standard solution gave $^{143}Nd/^{144}Nd$ of 0.512114 ± 0.000005 (2σ, n = 12), in full agreement with the recommended value of 0.512115 (Tanaka et al. 2000) and corresponding to an external reproducibility of ±0.09ε (2σ). Epsilon Nd values were calculated with the present-day chondritic (chondrite uniform reservoir) value of $^{143}Nd/^{144}Nd$ = 0.512630 (Bouvier et al. 2008). Neodymium depleted-mantle model ages ($T_{Nd,DM}$) were calculated following the approach described in De Paolo (1981), using mea-

sured Sm and Nd concentrations ($^{147}Sm/^{144}Nd$ = (Sm/Nd) × 0.6049) and present-day depleted-mantle values of $^{143}Nd/^{144}Nd$ = 0.51315 and $^{147}Sm/^{144}Nd$ = 0.2145. Isotope data, including results previously obtained on muds from the upper part of the Zambezi catchment (Garzanti et al. 2014a), are summarized in table 3. Geochemical data on all size fractions analyzed for isotope geochemistry and isotope geochemistry data are provided in full in tables A4 and A5.

Detrital Zircon Geochronology.   Detrital zircons were identified by automated phase mapping (Vermeesch et al. 2017) with a Renishaw inVia Raman microscope on the heavy-mineral separates of 18 samples, concentrated with standard magnetic techniques and directly mounted in epoxy resin without any operator selection by hand picking. U-Pb zircon ages were determined at the London Geochronology Centre with an Agilent 7700x LA-ICP-MS (laser ablation inductively coupled plasma mass spectrometry) system, employing a NewWave NWR193 Excimer Laser operated at 10 Hz with a 25-μm spot size and ~2.5-J/cm^2 fluence. No cathodoluminescence imaging was done, and the laser spot was always placed "blindly" in the center of zircon grains in order to treat all samples equally and avoid bias in intersample comparison ("blind-dating approach," as discussed in Garzanti et al. 2018). The mass spectrometer data were converted to isotopic ratios with the GLITTER 4.4.2 software (Griffin et al. 2008), employing Plešovice zircon (Sláma et al. 2008) as a primary age standard and GJ-1 (Jackson et al. 2004) as a secondary age standard. An NIST SRM612 glass was used as a compositional standard for the U and Th concentrations. GLITTER files were postprocessed in R with IsoplotR 2.5 (Vermeesch 2018). Concordia ages were calculated as the maximum likelihood intersection between the concordia line and the error ellipse of $^{207}Pb/^{235}U$ and $^{206}Pb/^{238}U$ (Ludwig 1998). The discordance cutoff was set at −5/+15 of the concordia distance (Vermeesch 2021). The complete geochronological data set, comprising 2095 concordant ages refined with a ^{208}Pb-based common Pb correction, is provided in appendix B.

Statistical Methods and Graphical Displays.   The relative contribution from each tributary or geological domain to the sediment flux of a trunk river can be quantified with forward-mixing models, provided that the compositional signatures of sediment in all potential sources are distinct and accurately determined (Weltje 1997; Garzanti et al. 2012). The forward-mixing model calculates a row vector of compositional data as a nonnegative linear combination between a matrix of fixed end-member

Table 2. Sand and Mud Geochemistry in the Zambezi Catchment

River	Major elements (wt%)										
	SiO_2	Al_2O_3	Fe_2O_3	MgO	CaO	Na_2O	K_2O	TiO_2	P_2O_5	MnO	LOI
Sand (63–2000 μm):											
Uppermost Zambezi	98.5	.4	.2	.03	.03	.02	.06	.07	.02	<.01	.8
Kasaya	99.2	.9	.1	.03	.1	.1	.4	.07	<.01	<.01	.9
Ngwezi	93.4	3.2	.4	.04	.5	.4	1.7	.04	<.01	.03	.5
Kwando	99.3	.2	<.04	<.01	<.01	<.01	<.01	.04	.01	<.01	.5
Chobe	98.0	.3	.9	.02	.02	<.01	.04	.08	<.01	<.01	.7
Upper Zambezi	98.9	.3	.1	.02	.02	.02	.06	.1	<.01	<.01	.9
Sinde	94.8	1.3	1.6	.3	.5	.2	.2	.4	.02	.02	.9
Zambezi above Victoria Falls	98.0	.6	.4	.05	.1	.06	.1	.2	.03	<.01	.6
Zambezi rapid #9	99.2	.8	.3	.07	.1	.1	.2	.2	<.01	<.01	.8
Zambezi rapid #19	99.4	.3	.3	.07	.1	.05	.05	.1	<.01	<.01	1.0
Masuie	61.8	8.3	12.9	3.1	4.9	1.5	.9	2.8	.19	.15	2.4
Upper Zambezi	99.7	.4	.4	.1	.2	.06	.05	.1	<.01	<.01	.8
Matetsi	63.1	8.4	11.7	3.1	5.0	1.7	.8	2.8	.23	.14	2.9
Zambezi above Kariba	89.7	3.9	2.0	.6	1.1	.8	.9	.5	.05	.02	.5
Umguza	85.4	5.4	2.0	.4	3.2	1.1	1.6	.2	.03	.07	3.2
Lower Gwai	88.3	7.1	.9	.2	.6	1.3	2.6	.1	.05	.02	.9
Kafue (FS)	83.0	6.2	3.5	1.0	1.2	1.0	1.7	.9	.10	.04	1.1
Kafue (VFS)	81.1	6.5	4.4	1.0	1.5	1.2	1.6	1.3	.13	.05	1.0
Middle Zambezi	80.6	8.0	3.3	1.1	1.3	1.5	2.3	.8	.11	.04	.9
Luangwa	89.9	4.7	1.2	.1	.3	.6	2.4	.2	.05	.02	.3
Mufa	71.3	11.8	3.9	1.8	3.7	2.4	2.9	.8	.18	.06	.9
Lower Zambezi at Tete	68.2	14.0	2.1	.9	3.2	3.2	2.8	.5	.16	.04	4.8
Morrunguze	52.4	12.5	15.1	3.9	5.5	2.4	1.5	5.5	.08	.17	.7
Luenha	74.5	10.7	5.1	.8	2.2	2.4	2.8	1.4	.08	.08	− .3
Mazowe	78.7	10.2	2.2	.6	1.7	2.2	3.3	.4	.07	.04	.5
Sangadze	82.1	8.5	1.5	.2	.9	1.3	4.2	.5	.07	.04	.6
Shire	68.3	14.7	3.8	1.3	3.9	3.7	2.1	.8	.20	.06	.9
Lower Zambezi (FS)	80.2	9.3	2.1	.6	1.8	2.0	2.6	.5	.10	.03	.7
Lower Zambezi (VFS)	78.1	10.4	2.3	.7	2.1	2.3	2.6	.6	.11	.04	.7
Mud (<32 μm):											
Uppermost Zambezi	55.4	15.0	7.0	.7	1.1	.2	1.0	.9	.13	.08	18
Kasaya	53.5	16.1	5.8	.8	1.8	.3	1.7	1.0	.41	.04	ND
Ngwezi	51.1	18.6	8.5	1.5	1.6	.6	2.1	1.1	.08	.12	15
Kwando	43.3	5.9	3.1	3.3	10.6	.07	.5	.4	.08	.21	30
Sinde	45.5	14.6	14.2	2.0	3.0	1.0	.9	3.5	.22	.18	15
Zambezi above Victoria Falls	54.0	10.6	7.3	1.4	2.7	.6	.8	1.8	.13	.08	20
Matetsi	44.4	14.2	12.2	3.7	6.2	1.7	.9	2.0	.39	.17	14
Zambezi above Kariba	50.7	12.7	10.1	2.1	3.1	.7	.9	1.5	.17	.22	18
Zambezi above Kariba	51.4	10.4	10.3	2.6	3.8	.8	.8	2.5	.18	.16	17
Umguza	51.0	15.0	8.8	2.0	3.0	.6	1.2	1.4	.21	.10	16
Upper Gwai	48.6	16.3	8.9	1.7	2.3	.4	1.5	1.2	.20	.22	18
Tinde	67.5	13.3	4.0	.8	.7	.7	2.5	.9	.09	.10	9
Kafue (VFS)	46.8	16.5	9.5	3.2	2.7	.8	2.9	1.3	.19	.12	15
Middle Zambezi	49.5	16.4	9.5	3.2	1.8	.8	2.9	1.3	.19	.13	14
Lower Zambezi at Tete	46.4	17.7	10.4	2.0	2.2	1.0	2.1	1.2	.30	.20	16
Sangadze	47.1	16.8	6.9	3.0	3.1	.4	1.9	.8	.23	.14	19
Shire	42.2	19.3	12.1	2.6	2.2	.9	1.9	1.3	.38	.15	17
Lower Zambezi (VFS)	48.3	16.3	11.6	2.9	2.4	1.0	2.4	1.5	.24	.15	13

River	Trace elements (ppm)											
	Rb	Sr	Ba	Sc	Y	Th	Zr	Hf	V	Nb	Cr	Ni
Sand (63–2000 μm):												
Uppermost Zambezi	2	3	29	<1	2	.8	81	2	14	1	<14	<20
Kasaya	11	18	124	<1	4	2	128	3	<8	2	<14	<20
Ngwezi	47	50	419	<1	5	1	38	1	11	2	14	<20
Kwando	1	2	21	<1	1	.4	62	2	<8	2	<14	<20
Chobe	2	4	29	<1	2	1	114	3	15	2	<14	<20
Upper Zambezi	2	4	31	<1	2	1	232	6	<8	2	<14	<20
Sinde	3	51	58	2	4	1	68	2	57	2	27	<20

Table 2 (*Continued*)

River	Trace elements (ppm)											
	Rb	Sr	Ba	Sc	Y	Th	Zr	Hf	V	Nb	Cr	Ni
Zambezi above Victoria Falls	3	11	52	<1	2	1	73	2	21	3	14	<20
Zambezi rapid #9	5	18	81	<1	2	1	62	2	14	3	<14	<20
Zambezi rapid #19	2	7	157	<1	1	1	31	1	11	2	21	<20
Masuie	18	268	295	22	23	2	168	4	414	10	96	78
Upper Zambezi	1	13	25	<1	2	0	37	1	16	1	<14	<20
Matetsi	16	365	296	20	22	2	182	5	356	13	109	70
Zambezi above Kariba	24	85	235	4	7	3	65	2	57	2	27	<20
Umguza	52	186	476	3	12	2	57	2	51	3	48	24
Lower Gwai	69	87	484	2	11	4	72	2	15	2	27	<20
Kafue (FS)	58	80	325	7	18	10	334	9	61	16	68	<20
Kafue (VFS)	52	92	316	8	28	16	596	16	84	24	68	<20
Middle Zambezi	74	122	415	7	18	8	294	8	58	15	55	<20
Luangwa	59	107	620	1	7	3	83	2	18	5	14	<20
Mufa	76	315	626	10	18	9	459	12	78	11	109	27
Lower Zambezi at Tete	70	313	695	6	15	4	125	3	39	5	68	23
Morrunguze	27	285	424	26	15	2	181	4	471	7	281	50
Luenha	74	168	552	8	21	32	348	9	89	25	55	<20
Mazowe	76	143	560	5	10	4	130	3	39	9	51	<20
Sangadze	103	237	1093	3	10	6	212	5	24	10	27	<20
Shire	35	585	995	10	14	2	268	7	78	11	55	21
Lower Zambezi (FS)	67	199	621	5	10	4	165	5	40	8	55	<20
Lower Zambezi (VFS)	69	200	616	6	15	6	153	4	41	9	68	<20
Mud (<32 μm):												
Uppermost Zambezi	53	54	301	17	34	11	246	8	134	15	89	34
Kasaya	147	84	459	16	37	22	372	9	122	19	109	43
Ngwezi	163	101	555	24	41	18	232	6	157	17	144	55
Kwando	44	339	707	6	14	6	170	5	82	8	55	34
Sinde	26	194	362	32	40	4	321	10	348	17	123	81
Zambezi above Victoria Falls	37	125	251	18	32	10	623	19	171	19	96	45
Matetsi	22	291	332	31	33	3	201	6	259	11	109	74
Zambezi above Kariba	51	137	374	21	33	9	274	8	211	15	103	55
Zambezi above Kariba	39	134	262	23	39	12	627	18	258	21	130	64
Umguza	55	147	303	22	25	6	175	4	196	10	137	77
Upper Gwai	75	125	410	22	30	10	200	6	174	13	137	70
Tinde	119	83	607	10	39	18	466	14	73	19	62	25
Kafue (VFS)	188	125	497	22	54	30	389	11	139	27	192	99
Middle Zambezi	184	113	512	22	57	31	489	13	144	28	171	91
Lower Zambezi at Tete	118	170	614	24	59	13	210	6	142	16	137	59
Sangadze	86	166	523	17	30	11	144	4	98	15	137	50
Shire	84	231	807	30	44	11	194	5	187	15	192	107
Lower Zambezi (VFS)	157	148	536	23	51	28	665	18	164	26	239	118

River	Weathering indices							
	CIA*	$\alpha^{Al}Mg$	$\alpha^{Al}Ca$	$\alpha^{Al}Na$	$\alpha^{Al}K$	$\alpha^{Al}Rb$	$\alpha^{Al}Sr$	$\alpha^{Al}Ba$
Sand (63–2000 μm):								
Uppermost Zambezi	77	1.8	3.0	4.1	1.2	1.0	3.1	.5
Kasaya	55	4.5	2.5	2.1	.4	.5	1.1	.3
Ngwezi	49	12.3	1.8	1.9	.4	.4	1.4	.3
Kwando	>89	>2.3	>4.4	>4.1	>3.6	1.4	2.1	.3
Chobe	78	2.1	3.4	ND	1.4	.9	1.6	.4
Upper Zambezi	75	2.5	4.2	3.9	1.1	1.1	1.9	.4
Sinde	47	.7	.6	1.5	1.6	2.5	.5	.8
Zambezi above Victoria Falls	63	1.7	1.4	2.1	1.0	1.2	1.1	.4
Zambezi rapid #9	58	1.9	1.6	2.0	.8	1.0	1.1	.4
Zambezi rapid #19	50	.7	.7	1.5	1.3	1.2	1.0	.1
Masuie	41	.4	.4	1.3	1.9	2.9	.7	1.1
Upper Zambezi	47	.6	.6	1.4	1.5	1.8	.6	.6
Matetsi	41	.4	.4	1.2	2.0	3.4	.5	1.1
Zambezi above Kariba	49	1.1	.9	1.2	.9	1.0	1.0	.6
Umguza	37	1.9	.4	1.2	.7	.7	.6	.4

Table 2 (*Continued*)

River	CIA*	$\alpha^{Al}Mg$	$\alpha^{Al}Ca$	$\alpha^{Al}Na$	$\alpha^{Al}K$	$\alpha^{Al}Rb$	$\alpha^{Al}Sr$	$\alpha^{Al}Ba$
				Weathering indices				
Lower Gwai	54	6.2	2.9	1.4	.6	.7	1.8	.5
Kafue (FS)	53	.9	1.5	1.5	.8	.7	1.8	.7
Kafue (VFS)	52	1.0	1.2	1.4	.9	.9	1.6	.7
Middle Zambezi	53	1.1	1.7	1.4	.8	.7	1.5	.7
Luangwa	54	5.7	3.9	1.9	.4	.5	1.0	.3
Mufa	47	.9	.9	1.3	.9	1.0	.9	.7
Lower Zambezi at Tete	50	2.2	1.2	1.1	1.1	1.4	1.0	.7
Morrunguze	45	.5	.6	1.4	1.8	3.2	1.0	1.1
Luenha	50	1.9	1.3	1.1	.9	1.0	1.5	.7
Mazowe	50	2.7	1.7	1.2	.7	.9	1.6	.7
Sangadze	51	8.2	2.7	1.7	.4	.6	.8	.3
Shire	50	1.6	1.0	1.0	1.5	2.9	.6	.5
Lower Zambezi (FS)	51	2.3	1.4	1.2	.8	.9	1.1	.5
Lower Zambezi (VFS)	51	2.1	1.4	1.2	.9	1.0	1.2	.6
Mud (<32 μm):								
Uppermost Zambezi	83	2.9	3.7	21.4	3.3	1.9	6.4	1.8
Kasaya	78	3.0	2.5	14.2	2.1	.7	4.4	1.3
Ngwezi	76	1.8	3.3	8.2	1.9	.8	4.2	1.2
Kwando	23	.3	.2	21.7	2.9	.9	.4	.3
Sinde	66	1.1	1.4	3.7	3.4	3.8	1.7	1.5
Zambezi above Victoria Falls	62	1.1	1.1	4.6	3.1	1.9	2.0	1.5
Matetsi	50	.6	.6	2.2	3.3	4.4	1.1	1.5
Zambezi above Kariba	63	.9	1.1	4.6	3.1	1.7	2.1	1.2
Zambezi above Kariba	55	.6	.8	3.3	2.8	1.8	1.8	1.4
Umguza	67	1.1	1.4	6.4	2.8	1.9	2.4	1.8
Upper Gwai	73	1.4	1.9	10.5	2.4	1.5	3.0	1.4
Tinde	73	2.4	5.2	5.2	1.2	.8	3.7	.8
Kafue (VFS)	65	.7	1.7	5.3	1.3	.6	3.0	1.2
Middle Zambezi	69	.7	2.6	5.0	1.3	.6	3.4	1.2
Lower Zambezi at Tete	71	1.3	2.3	4.4	1.8	1.0	2.4	1.0
Sangadze	68	.8	1.5	9.8	2.0	1.3	2.3	1.2
Shire	75	1.1	2.5	5.6	2.2	1.6	1.9	.9
Lower Zambezi (VFS)	67	.8	1.9	4.3	1.5	.7	2.5	1.1

Note.   FS = fine sand; VFS = very fine sand; LOI = loss on ignition; ND = not determined. CIA* (chemical index of alteration) values are corrected only for CaO in apatite. The α values are defined as $(Al/E)_{sample}/(Al/E)_{UCC}$, where UCC = upper continental crust.

compositions and a row vector of coefficients representing the proportional contribution of each end member to the observation. The accuracy of calculations depends on how distinct and precisely assessed the end-member signatures of all potential sources are. Additional information on the method is contained in appendix A and Resentini et al. (2017).

Statistical techniques used to illustrate our data sets include the compositional biplot (Gabriel 1971; Aitchison and Greenacre 2002) and multidimensional scaling (MDS; Vermeesch 2012; Vermeesch and Garzanti 2015). The compositional biplot (drawn with CoDaPack software; Comas and Thió-Henestrosa 2011) allows discrimination among multivariate observations (points) while shedding light on the mutual relationships among multiple variables (rays). The length of each ray is proportional to the variance of the corresponding variable; if the angle between two rays is 0° or 180°, then the corresponding variables are perfectly correlated or anticorrelated. MDS analysis produces a map of points in which the distance among samples is approximately proportional to the Kolmogorov-Smirnov dissimilarity of their compositional or chronological signatures. The goodness of fit is evaluated using the "stress" value of the configuration (20 = poor; 10 = fair; 5 = good; Kruskal and Wish 1978). The provenance package of Vermeesch et al. (2016) was used to plot MDS maps and U-Pb age distributions as kernel density estimates.

Data

This section briefly summarizes petrographic and heavy-mineral data (provided in full in tables A6

Table 3. Neodymium Isotope Values and Sm-Nd Model Ages for Cohesive-Mud (<32-μm), Very Coarse Silt (32–63-μm), and Sand (63–2000-μm) Fractions of Zambezi Sediments

River	ε_{Nd}			T_{DM} (Ma)		
	<32 μm	32–63 μm	63–2000 μm	<32 μm	32–63 μm	63–2000 μm
Uppermost Zambezi[a]	−15.5	ND	ND	2162	ND	ND
Kasaya[a]	−14.0	ND	ND	2006	ND	ND
Ngwezi[a]	−15.6	ND	ND	2128	ND	ND
Kwando[a]	−17.3	ND	ND	2320	ND	ND
Sinde[a]	−5.3	ND	ND	1608	ND	ND
Zambezi at Victoria Falls[a]	−12.5	ND	ND	2056	ND	ND
Matetsi[a]	−4.1	ND	ND	1454	ND	ND
Upper Zambezi[a]	−12.0	ND	ND	2010	ND	ND
Upper Zambezi[a]	−12.5	ND	ND	2092	ND	ND
Umguza[a]	−14.7	ND	ND	2177	ND	ND
Upper Gwai[a]	−11.6	ND	ND	1872	ND	ND
Tinde[a]	−14.4	ND	ND	1953	ND	ND
Gwai	ND	ND	−24.6	ND	ND	2690
Kafue (FS)	ND	−16.5	−17.7	ND	2029	2107
Kafue (VFS)	−14.8	−16.4	−15.0	1935	1976	1762
Middle Zambezi	−13.8	−16.2	−14.5	1925	2084	2106
Luangwa	ND	−20.1	−16.5	ND	2244	2155
Mufa	ND	ND	−8.8	ND	ND	2195
Lower Zambezi at Tete[b]	−7.8	−7.7	−10.0	1552	1864	1735
Morrunguze	ND	ND	−1.9	ND	ND	1162
Mazowe	ND	ND	−18.2	ND	ND	2781
Luenha	ND	ND	−19.4	ND	ND	2504
Sangadze	−15.3	−21.1	−19.5	1887	2028	2094
Shire	−7.3	−8.0	−7.7	1279	1333	1455
Lower Zambezi (FS)	−16.0	−19.3	−14.8	1995	2221	2188
Lower Zambezi (VFS)	−14.3	−17.4	−14.5	1990	2242	2242
Quelimane (estuary)	ND	ND	−18.3	ND	ND	2319
Quelimane (beach)	ND	ND	−12.7	ND	ND	1968

Note.   Except as noted, data are from sand samples. FS = fine sand; VFS = very fine sand; ND = not determined.
[a] Data are from mud samples collected in the upper part of the Zambezi catchment, after Garzanti et al. (2014*a*).
[b] Lower Zambezi silt.

and A7 and illustrated in detail in the companion paper, Garzanti et al. 2021*b*) and presents new data on clay mineralogy (table 1; fig. 3), elemental geochemistry for mud and sand samples (table 2; fig. 4), rare earth element (REE) geochemistry (fig. 5), Nd isotope geochemistry (table 3; fig. 6), and detrital zircon geochronology (table 4; fig. 7) from the whole Zambezi River sedimentary system.

Five main zircon age ranges recur among the analyzed samples, corresponding to main thermal events of crustal growth across southern Africa (Hanson 2003; Dirks et al. 2009; Andersen et al. 2016, 2018): (1) "Karoo" (Triassic–Permian, 253 ± 21 Ma), (2) "Pan-African" (Cambrian–Ediacaran, 571 ± 22 Ma, and Tonian, 792 ± 54 Ma), (3) "Irumide" (Stenian, 1036 ± 32 Ma), (4) "Eburnean" (Orosirian, 1947 ± 70 Ma), and (5) "Limpopo" (late Neoarchean, 2568 ± 47 Ma; table 4). A few zircon ages referred to the Ectasian "Kibaran" (~1.35 Ga) or Calymmian/Statherian "Lukamfwa" events (~1.55 Ga; De Waele et al. 2003) are recorded mainly in the Upper Zambezi catchment and Luangwa sand. The youngest zir-

con ages (103–121 Ma) were obtained from lowermost Zambezi sands.

The Uppermost Zambezi. Uppermost Zambezi and Kwando sands are pure quartzose. Sands of the left Zambian tributaries range from quartz-rich feldspathoquartzose (Kabombo, Ngwezi) to pure quartzose (Kasaya). Smectite prevails over kaolinite and mica/illite in mud of the Zambezi main stem and is dominant in Ngwezi and Kwando muds (fig. 3).

In Zambezi and Kwando sands, SiO_2 is overwhelming (>98%; fig. 4*A*) and other elements very low, including Zr (62–114 ppm) and REEs (fig. 5). The CIA* is ≥77, the WIP is <1, $\alpha^{Al}Ca \geq 3$, and $\alpha^{Al}Na \sim 4$. Ngwezi sand is less SiO_2 rich, with higher Al, Ca, Na, K, Rb, Sr, and Ba but very low Mg (fig. 4*B*). Kasaya sand has an intermediate composition. Chemical indices are CIA* = 83, $\alpha^{Al}Ca = 4$, $\alpha^{Al}Na = 21$ for Zambezi mud and CIA* = 77 ± 1, $\alpha^{Al}Ca = 2.9 \pm 0.5$, and $\alpha^{Al}Na = 11 \pm 4$ for Kasaya and Ngwezi muds. Kwando mud has anomalously low $\alpha^{Al}Ca$, $\alpha^{Al}Mg$, $\alpha^{Al}Sr$, and $\alpha^{Al}Ba$ (table 2).
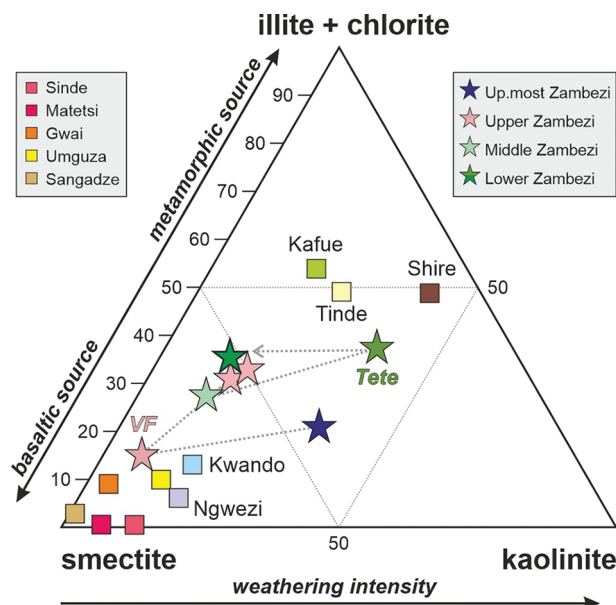
Figure 3. Clay mineralogy. Multiple controls explain erratic trends (dotted arrow) downstream the Zambezi River (stars). Recycled kaolinite occurs in both Uppermost (Up.most) Zambezi and Lower Zambezi catchments (e.g., Shire mud). Smectite is derived from Karoo basalt around Victoria Falls (VF) but is also produced on the Kalahari Plateau and Mozambican lowlands (e.g., Sangadze mud). Illite is derived from metasedimentary and siliciclastic rocks of the Irumide and Pan-African belts (e.g., Kafue and Tinde muds).

The general observed order of element mobility is Na $\gg$ Sr > Ca > Mg$\approx$K for mud and Na$\approx$Ca > Sr for sand. In mud samples, REE patterns normalized to CI carbonaceous chondrites (Barrat et al. 2012) display classical shapes with higher light-REE (LREE) than heavy-REE (HREE) fractionation and moderately negative Eu anomaly. Pure quartzose sands display slightly stronger LREE enrichment, negative Ce anomalies, more strongly negative Eu anomalies, and low HREE fractionation. The ε_{Nd} values vary between -14 and -17 (-15.5 for Uppermost Zambezi mud; table 3).

Ages of zircon grains in Uppermost Zambezi, Kwando, and Kasaya sands display polymodal spectra, with mostly Cambrian to Stenian ages, including a main Irumide and subordinate Pan-African peaks (fig. 7). Orosirian ages are common in Uppermost Zambezi and Kwando sands and minor in Kasaya sand. Kwando sand is distinguished by a Neoarchean age cluster, whereas Kasaya sand yielded several zircon grains with Devonian to Triassic ages.

The Upper Zambezi. Zambezi sand becomes rapidly enriched in basaltic detritus downstream of Victoria Falls. Bedload sand and levee silty sand

upstream of Lake Kariba are, respectively, quartzose and plagioclase-rich litho-feldspathoquartzose with mafic volcanic rock fragments and green augite. Basaltic detritus increases from west to east also in Zambezi tributaries, from quartzose Sinde sand to lithic-rich lithoquartzose and quartzolithic Masuie and Matetsi sands containing common augite. Smectite predominates over mica/illite and kaolinite in Zambezi mud and is overwhelming in muds of the Sinde and Matetsi tributaries, which contain kaolinite (fig. 3).

Silica decreases progressively along the Upper Zambezi, with corresponding increases in most other elements, including Fe, Mg, Ca, Na, Sr (fig. 4G, 4H), and REEs (fig. 5C) but not Zr, Hf, and Nb. Chemical indices upstream of Lake Kariba are CIA* = 59 $\pm$ 6, $\alpha^{Al}Ca$ = 0.9 $\pm$ 0.3, and $\alpha^{Al}Na$ = 3.9 $\pm$ 0.9 for mud; CIA* = 45, $\alpha^{Al}Ca$ = 0.5, and $\alpha^{Al}Na$ = 1.5 for silty sand; and CIA* = 49, $\alpha^{Al}Ca$ = 0.9, and $\alpha^{Al}Na$ = 1.2 for sand. Tributaries draining progressively larger portions of Karoo basalts display an even sharper trend from west to east. Masuie and Matetsi sands have much lower SiO$_2$ than Sinde sand and higher concentrations of all other elements (fig. 4A). In these rivers, both mud and sand are markedly enriched in Mg, Ca, Sc, Ti, V, Cr, Fe, Mn, Co, Ni, and Cu (fig. 4B) and display regular chondrite-normalized REE patterns lacking an Eu anomaly (fig. 5A, 5D, and 5G). The ε_{Nd} value is around -12 in Zambezi mud between Victoria Falls and Lake Kariba and is much less negative for Matetsi (-4) and Sinde (-5) muds.

Sinde sand yielded a zircon age spectrum with a dominant Irumide peak, common Neoproterozoic ages, and minor Permian–Triassic, Eburnean, and Neoarchean ages. Upper Zambezi sand upstream of Lake Kariba yielded a polymodal spectrum with main Pan-African and Irumide peaks and minor Orosirian and Neoarchean clusters (fig. 7).

Lower Gwai sand is feldspathoquartzose, with biotite and amphibole. Smectite predominates in upper Gwai and Umguza muds, whereas mica/illite prevails over kaolinite and smectite in mud of the lower-course Tinde tributary (fig. 3). Chemical indices are CIA* = 73, $\alpha^{Al}Ca$ = 1.9, and $\alpha^{Al}Na$ = 10 for upper Gwai mud and CIA* = 54, $\alpha^{Al}Ca$ = 2.9, and $\alpha^{Al}Na$ = 1.4 for lower Gwai sand. Umguza mud is similar to upper Gwai mud, whereas Umguza sand is much richer in Fe, Mg, Ca, Ti, Mn, Sr, V, Co, Ni, and Cu than lower Gwai sand (fig. 4C, 4D). Tinde mud is richer in Si, Na, K, Rb, Ba, Y, REEs, Th, U, Zr, Hf, Nb, and Ta and poorer in Fe, Mg, Ca, P, Mn, Sc, V, Cr, Co, Ni, and Cu (table 2). The ε_{Nd} value ranges between -12 and -15 in upper Gwai, Umguza, and Tinde muds, but it is strongly negative
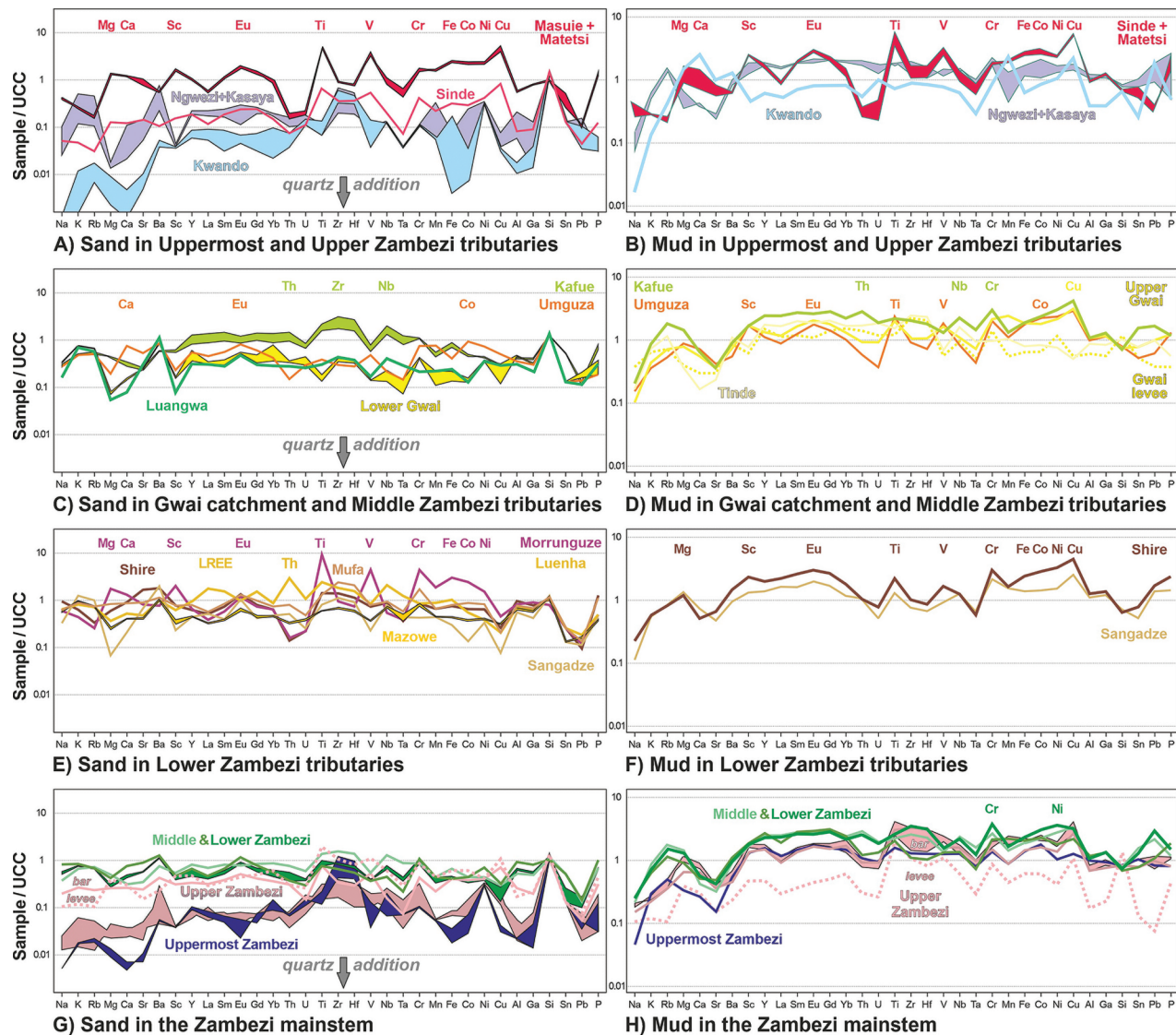
Figure 4. Sand and mud geochemistry (in UCC [upper continental crust]-normalized diagrams, chemical elements are arranged following the periodic table group by group). *A*, *B*, In Zambezi headwaters, extensive quartz addition by recycling explains relative depletion of most elements other than Si in sand. Supply from Karoo basalt leads to marked increase in ferromagnesian metals and lack of an Eu anomaly. High Ca, Sr, Mg, and Ba in Kwando mud reflect reworking of calcrete soils. *C*, *D*, Kafue samples are slightly enriched in elements hosted in ultradense minerals. Umguza and Upper Gwai sediments include minor detritus from Karoo basalt. Luangwa sand is partly recycled from Karoo siliciclastic strata. *E*, *F*, Most Lower Zambezi tributaries carry sediment that is undepleted relative to the UCC. In Morrunguze sand, high ferromagnesian metals and lack of an Eu anomaly reflect supply from the Tete gabbro-anorthosite. High light rare earth elements (LREE) and Th in Luenha sand suggest presence of monazite. *G*, *H*, Recycled quartz decreases downstream the Zambezi main stem. Lower Zambezi sand is only moderately depleted relative to the UCC, and mud is undepleted.

in Gwai sand upstream of lake Kariba (−25), which yielded a polymodal zircon age spectrum with major Neoarchean and Eburnean peaks and minor Irumide and Pan-African peaks (fig. 7).

The Middle Zambezi. Between Lakes Kariba and Cahora Bassa, Zambezi sand has the same feldspar-rich feldspathoquartzose composition as Kafue sand,

with metamorphic rock fragments, mica, and amphibole. The Luangwa River carries feldspathoquartzose sand with granitoid to gneissic rock fragments and amphibole. Smectite predominates over mica/illite and kaolinite in mud of the Zambezi main stem, whereas mica/illite predominates over smectite and kaolinite in Kafue mud (fig. 3).
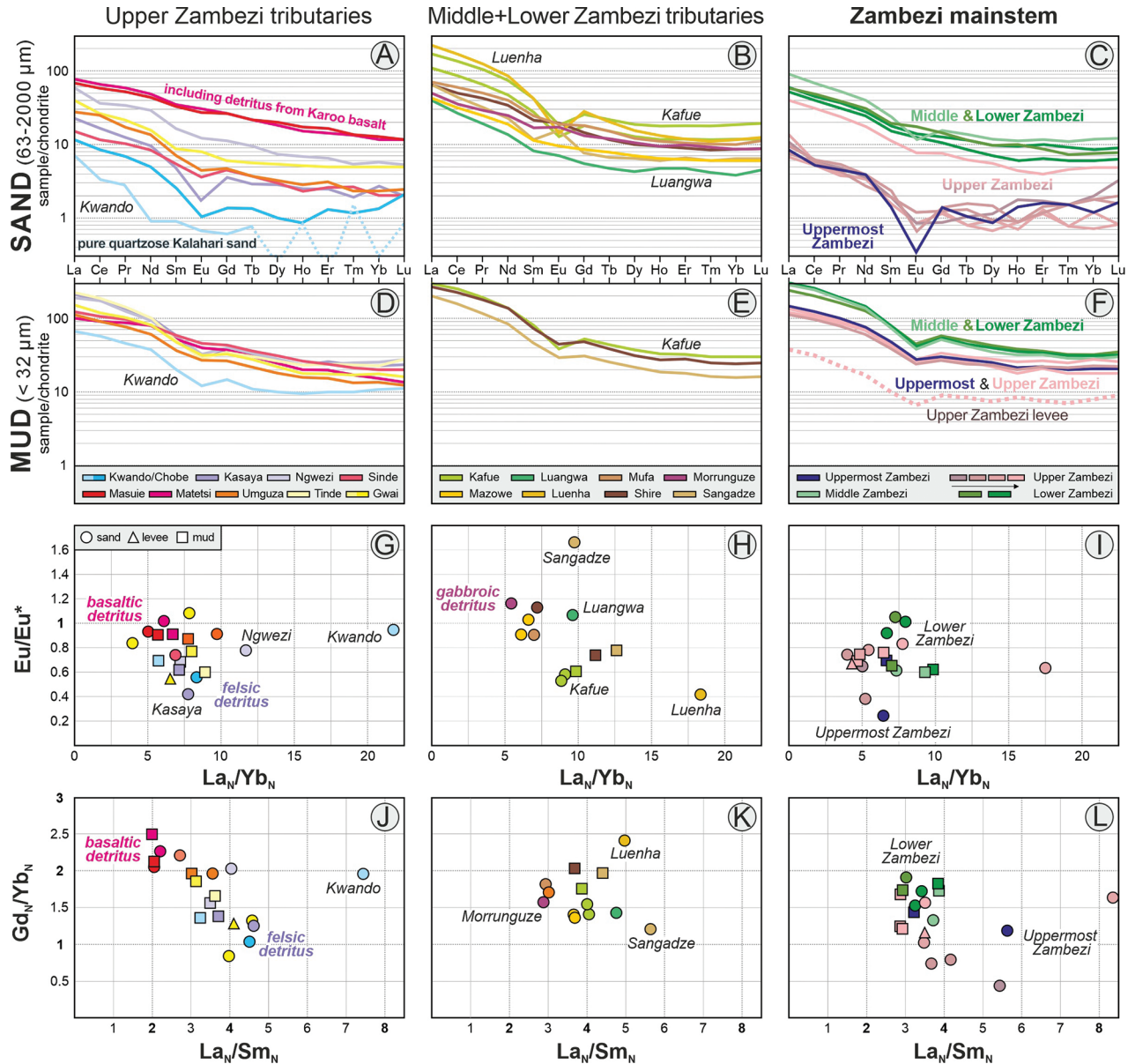
Figure 5. Rare earth elements (REEs). *A–C*, Chondrite-normalized REE patterns for sand. HREE (heavy-REE) trends are ill defined in pure quartzose sand because of very low concentration of elements with odd atomic numbers (Tb, Ho, Tm, Lu). *D–F*, Chondrite-normalized REE patterns for mud. *G–I*, La_N/Yb_N versus Eu anomaly. *J–L*, LREE (light-REE) versus HREE fractionation. Mafic detritus, conspicuous in Matetsi, Masuie, and Morrunguze sediments and present in Sinde, Umguza, and Upper Zambezi sediments, has higher REE concentration, lower LREE fractionation, no Eu anomaly, and higher HREE fractionation. Absence of an Eu anomaly in most Lower Zambezi sands reflects abundance of Ca-bearing feldspar. The steepest REE patterns with a strongly negative Eu anomaly in Luenha sand indicate the presence of monazite, whereas the strongly positive Eu anomaly in Sangadze sand reflects abundant feldspar with lesser quantities of heavy minerals.

Chemical indices are CIA* = 67 ± 3, $\alpha^{Al}Ca$ = 2.1 ± 0.6, and $\alpha^{Al}Na$ = 5.2 ± 0.2 for mud and CIA* = 51 ± 3, $\alpha^{Al}Ca$ = 2.1 ± 1.3, and $\alpha^{Al}Na$ = 1.6 ± 0.2 for sand. The observed order of element mobility is Na > Sr > Ca > K > Ba for mud and Ca > Na > Sr for sand. Luangwa sand is higher in

SiO_2, K, and Ba and lower in most other elements (especially Mg, Ti, and Sc; fig. 4*C*). The finer-grained of the two Kafue sand samples is notably enriched in Zr, Hf, REEs, Th, U, Nb, and Ta (table 2). Kafue and Middle Zambezi muds have virtually identical chemical compositions (fig. 4*D*, 4*H*). All ε_{Nd} values
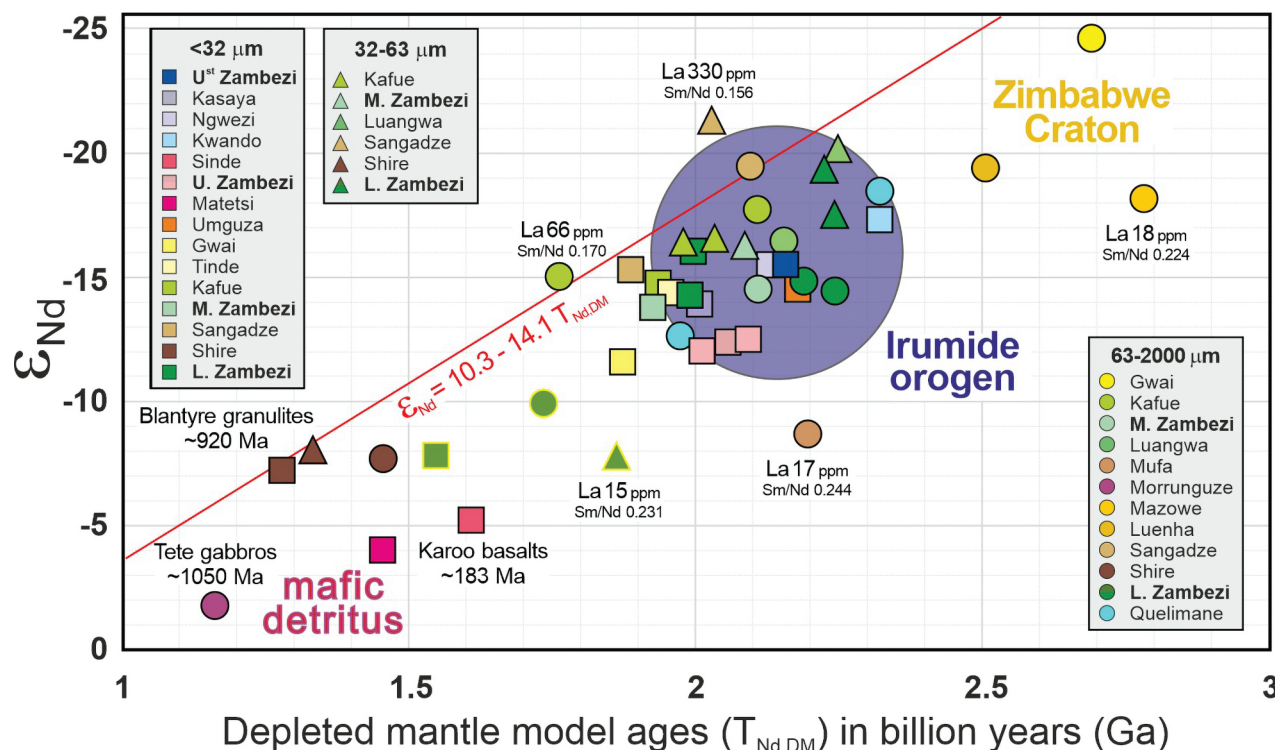
Figure 6. Relationship between $\varepsilon_{Nd(0)}$ and depleted-mantle model ages ($T_{Nd,DM}$) for the Zambezi main stem and tributaries. The ε_{Nd} and $T_{Nd,DM}$ values are least negative and youngest for detritus from Karoo basalt, Tete gabbro, and Blantyre mafic granulite (emplacement ages after Svensen et al. 2012, Westerhof et al. 2008, and Goscombe et al. 2020, respectively) and most negative and oldest for detritus from Neoarchean cratonic gneiss. Most samples have higher Sm/Nd ratios than the upper continental crust and thus plot to the right of the red line (based on $(Sm/Nd)_{UCC}$ = 0.1735). The 32–63-μm size class of sand samples, representing the fine tail of the size distribution, where ultradense monazite is concentrated, has high LREEs (light rare earth elements) and a steeper LREE pattern (lower Sm/Nd) than the 63–2000-μm fraction. Instead, the 32–63-μm size class of the Lower Zambezi silt collected at Tete (yellow outline) has low LREEs and a high Sm/Nd because it represents the coarse tail of the size distribution depleted in ultradense minerals. U^{st} = uppermost; U. = upper; M. = middle; L. = lower.

range between −14 and −18, reaching −20 only in the 32–63-μm size class of Luangwa sand.

The zircon age spectrum of Kafue sand displays a dominant Irumide peak with a minor Pan-African cluster and a few Triassic and Paleoproterozoic to Neoarchean ages. Luangwa sand is characterized by a trimodal spectrum with major Irumide, subordinate Pan-African, and minor Eburnean peaks and a few Permian ages (fig. 7).

The Lower Zambezi. In Mozambique, Zambezi sand ranges from quartzofeldspathic to feldspar-rich feldspathoquartzose with biotite, amphibole, and garnet. Most tributaries carry quartzofeldspathic sand with amphibole, garnet, clinopyroxene, hypersthene, and epidote. Feldspar (mostly plagioclase) is twice as abundant as quartz in Shire sand from Malawi. Metabasite grains are common in Morrunguze sand. Kaolinite, mica/illite, and smectite occur in subequal amounts in Zambezi mud collected at

Tete, whereas smectite predominates over mica/illite and kaolinite is subordinate upstream of the delta (fig. 3). Sangadze mud consists almost exclusively of smectite, whereas Shire mud contains mica/illite and kaolinite in subequal proportions (table 1).

Chemical indices are remarkably constant in sediments of the Zambezi main stem and most of its main tributaries (CIA^* = 70 ± 3, $\alpha^{Al}Ca$ = 2.0 ± 0.4, and $\alpha^{Al}Na$ = 6.0 ± 2.6 for mud; CIA^* = 50.4 ± 0.4, $\alpha^{Al}Ca$ = 1.6 ± 0.5, and $\alpha^{Al}Na$ = 1.2 ± 0.2 for sand; table 2). Plagioclase abundance explains why an Eu anomaly is not shown (fig. 5H, 5I). The observed order of element mobility is Na > Sr > Ca > K > Rb for mud and Ca > Na > Sr for sand. In all grain-size fractions of Lower Zambezi sediments, ε_{Nd} values become much more negative from Tete to upstream of the delta, where the very-fine-sand sample yielded a less negative value than the fine-sand sample (table 3).

Table 4. U-Pb Age Peaks (Peak) of Detrital Zircons and Relative Frequencies (Freq.) in Modern Sands of the Zambezi Catchment

River	Karoo Peak (Ma)	Freq. (%)	Pan-African II Peak (Ma)	Freq. (%)	Pan-African I Peak (Ma)	Freq. (%)	Irumide Peak (Ma)	Freq. (%)	Lukamfwa Peak (Ma)	Freq. (%)	Eburnean Peak (Ma)	Freq. (%)	Limpopo Peak (Ma)	Freq. (%)
Uppermost Zambezi	235 ± 14	2	561 ± 10	27			1009 ± 15	39			1989 ± 31	32		
Kasaya	281 ± 12	8	558 ± 10	34			1100 ± 16	45			2064 ± 58	13		
Kwando			575 ± 11	27			990 ± 17	36			1891 ± 36	25	2571 ± 78	12
Sinde	255 ± 9	7	570 ± 16	15	816 ± 30	15	1079 ± 21	42			1968 ± 46	21		
Upper Zambezi			593 ± 11	33			987 ± 20	34			1905 ± 46	24	2578 ± 103	9
Gwai	243 ± 11	4	589 ± 12	19			1064 ± 23	17			2028 ± 40	29	2606 ± 52	31
Kafue	230 ± 13	3	616 ± 22	11			1035 ± 12	79			1866 ± 87	5	2579 ± 205	2
Luangwa			550 ± 15	20	717 ± 39	8	1066 ± 17	54	1530 ± 76	8	1998 ± 82	10		
Sangara							1061 ± 8	100						
Mufa			559 ± 19	13	754 ± 50	12	1002 ± 14	75						
Morrunguze							1030 ± 18	100						
Mazowe			555 ± 14	14	844 ± 10	57							2518 ± 41	29
Luenha			529 ± 18	12	831 ± 12	58							2529 ± 49	30
Shire			564 ± 8	46			1022 ± 13	54						
Zangue			560 ± 18	55			1036 ± 42	33			1926 ± 197	6	2676 ± 274	6
Lower Zambezi			597 ± 15	17			1013 ± 11	72			1851 ± 82	6	2522 ± 91	5
Lower Zambezi			587 ± 11	21			1039 ± 12	49			1878 ± 35	22	2545 ± 42	8
Praia da Madal	272 ± 14	4			686 ± 27	21	1044 ± 15	56			1998 ± 53	17	2558 ± 72	2

Note. Ages and frequencies are calculated with Density Plotter (Vermeesch 2012). To treat all samples equally and avoid bias in intersample comparison, the laser spot was always placed blindly in the center of zircon grains.
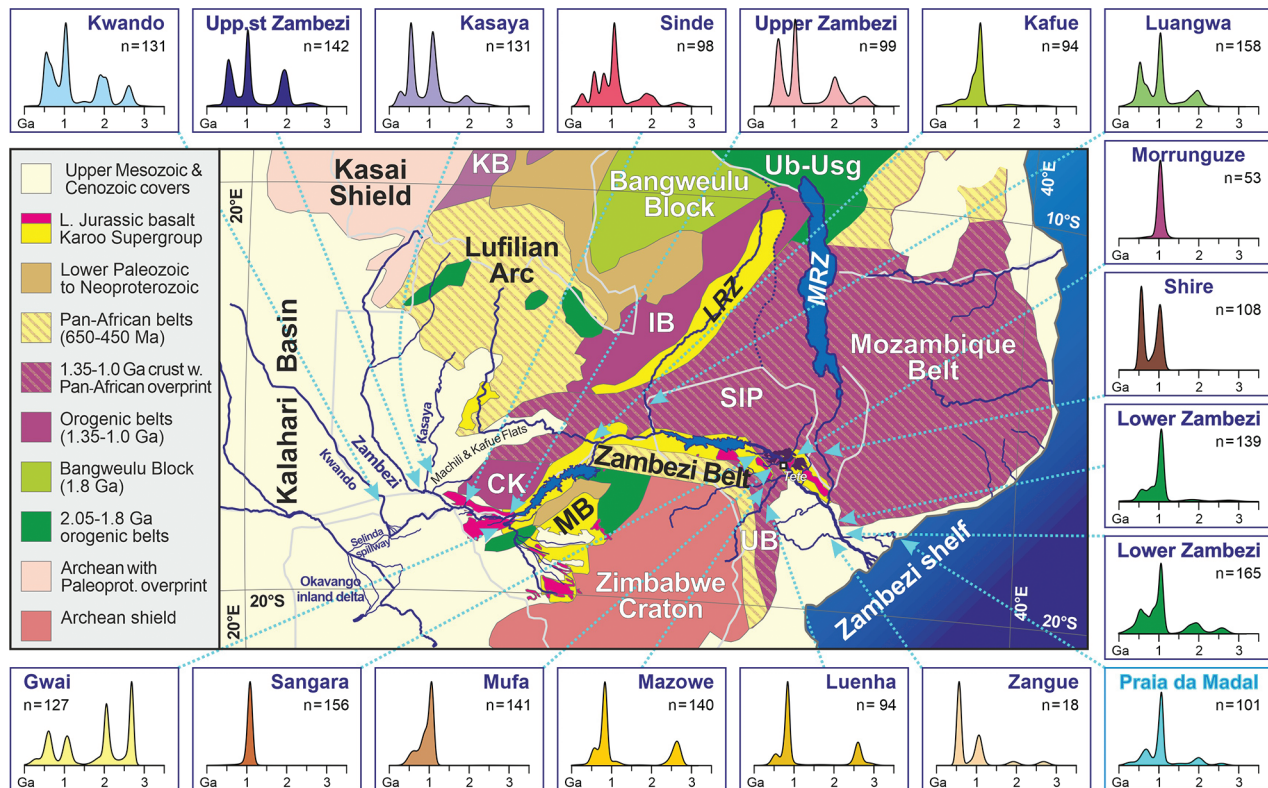
Figure 7. U-Pb age spectra of detrital zircons. Archean ages are common in Gwai, Mazowe, and Luenha sands sourced in the Zimbabwe Craton. Orosirian ages are common in Kwando and Uppermost (Upp.st) Zambezi sands recycling Kalahari dunes and in Gwai sand largely derived from the Paleoproterozoic (Paleoprot.) Magondi Belt. Irumide ages are widespread, overwhelming in Sangara and Morrunguze sands and dominant in Lower Zambezi sand. Pan-African zircons are also widespread, but only locally prevalent (Shire and Zangue sands). Geological domains are after Hanson (2003) and Thiéblemont et al. (2016). CK = Choma-Kalomo Block; IB = Irumide Belt; KB = Kibaran Belt; LRZ = Luangwa Rift Zone; MB = Magondi Belt; MRZ = Malawi Rift Zone; SIP = southern Irumide Province; UB = Umkondo Belt; Ub-Usg = Ubendian-Usagaran Belts; L. Jurassic = Lower Jurassic.

Sand of the Morrunguze River, draining gabbroic rocks of the Tete Complex, is low in SiO_2 (52%), K, and Rb and notably rich in Fe, Mg, Ca, Ti, Mn, Sc, V, Cr, Co, Ni, and Cu (fig. 4E) and yielded the least negative ε_{Nd} value (fig. 6). Mufa sand, enriched in the same elements but to a much lesser extent, yielded high Zr and Hf concentrations (table 2) and a more negative ε_{Nd} value. Luenha sand is relatively rich in Zr, Hf, U, Nb, Ta, and REEs, is the richest in Th (fig. 4E), displays the steepest REE patterns with the largest negative Eu anomaly (fig. 5H, 5K), and is the only sample with negative loss on ignition (LOI; −0.3). Mazowe and Luenha sands have ε_{Nd} values of −18 and −19, respectively. Shire sand is highest in Al, Na, Sr, and P and shows a much less negative ε_{Nd} value (fig. 7). Sangadze sand is the richest in K, Rb, and Ba and displays a strongly positive Eu anomaly (fig. 5H)—reflecting abundant feldspar

and fewer heavy minerals—and a strongly negative ε_{Nd} value. Shire mud is low in SiO_2 (42%) and highest in Al, Fe, Sr, Ba, P, Sc, V, and Cu (fig. 4F). Zambezi mud upstream of the delta is high in Zr, Hf, REEs, Th, U, Nb, Ta, Cr, Mo, W, Co, and Ni (fig. 4H) and displays a negative Eu anomaly (fig. 5I).

The U-Pb age spectrum of zircon grains supplied by the Zambezi River to the delta displays a dominant Irumide peak, with common Neoproterozoic, some Orosirian, and a few Neoarchean and late Paleozoic ages (fig. 7). Sangara and Morrunguze zircons show a unimodal Irumide peak, which is associated with minor Neoproterozoic ages in Mufa sand. Luenha and Mazowe sands yielded nearly identical bimodal zircon age spectra with Neoproterozoic and Neoarchean peaks (table 4). The spectrum of Shire sand is also bimodal but with Irumide and Pan-African peaks. Pan-African

ages are more common than Irumide ages in Zangue sand (fig. 7).

The Northern Zambezi Delta. Estuary and beach sand ~100 km north of the Zambezi mouth is feldspathoquartzose with amphibole, epidote, and clinopyroxene. The ε_{Nd} value of bulk sand ranges between −13 and −18. The U-Pb zircon age spectrum displays a dominant Irumide peak with common Neoproterozoic, some Orosirian, and a few Neoarchean and Permian ages, similar to Lower Zambezi sand (fig. 7).

Provenance Insights from Clay Mineralogy and Sediment Geochemistry

Clay mineralogy and sediment geochemistry are largely controlled by factors other than provenance. If weathering is intense, then they reflect the lithology of source rocks only poorly, which explains why they have long been used to evaluate weathering rather than provenance (e.g., Nesbitt and Young 1982; Velde and Meunier 2008). However, despite the complexities associated with multiple controls on sediment composition (Johnsson 1993), clay minerals and elemental and especially isotope geochemistry do offer complementary information useful to augment the completeness and robustness of provenance analysis, for several reasons (McLennan et al. 1993). First, most other provenance techniques are best suited to tackle sand and, in the case of detrital geochronology, only a millesimal fraction of total sand. Geochemistry, instead, can be applied to bulk sediment samples of any size fraction from clay to granule. This allows us to investigate almost the entirety of the sediment flux, including clay and silt, which constitute the large majority of the detrital mass transported in river systems as suspended load (e.g., Hay 1998; Milliman and Farnsworth 2011). The aim of this section is thus to complement previous considerations based only on sand with inferences derived independently from the mineralogy and geochemistry of mud.

Clay Minerals. The clay mineralogy of unconsolidated mud depends on weathering processes in soils but reflects provenance as well, especially in dry climates where illite and chlorite are largely derived from phyllosilicate-rich metamorphic bedrock, whereas smectite is shed by mafic lava (e.g., Chamley 1989). Among the studied samples, smectite is the dominant clay mineral (≥87%) in mud transported by the Sinde and Matetsi tributaries of the Upper Zambezi and by the Umguza tributary of the Gwai River, all partly draining Karoo basalt between southern Zambia and western Zimbabwe.

Smectite, however, is also produced in abundance in regions lacking significant exposures of mafic rocks (e.g., the Kwando catchment) and represents the virtually exclusive clay mineral in mud of the Sangadze River flowing across Mozambican lowlands, indicating incomplete flushing of mobile ions in poorly drained low-relief regions (Wilson 1999). Illite is the most abundant clay mineral in mud of the Kafue and Shire Rivers, chiefly draining Proterozoic metamorphic basement, and in mud of the Tinde River, draining Neoproterozoic molasse (fig. 3).

Sand Geochemistry. The piece of provenance information most readily obtained from geochemical data is the supply from mafic rocks, revealed by high concentrations of ferromagnesian metals, including Mg, Sc, Ti, V, Cr, Mn, Fe, Co, and Ni (fig. 8; McLennan et al. 1993; von Eynatten et al. 2003). Among the analyzed samples, these elements reach the highest values in Masuie and Matetsi sands, draining Karoo basalts, and in Morrunguze sand, draining the Tete gabbro-anorthosite (fig. 4). Intermediate values for these elements are obtained for the Sinde and Umguza Rivers and for the Middle Zambezi upstream of Lake Kariba, all draining Karoo basalts more marginally (table 2). Other samples in the Upper Zambezi catchment have $SiO_2 > 90\%$, revealing extensive recycling of pure quartzose Kalahari sand.

The virtually identical chemical composition of Kafue and Middle Zambezi muds confirms that the Kafue is by far the most important source of sediment to the Middle Zambezi between Lake Kariba and the Luangwa confluence. Slightly above 80% in Kafue and Middle Zambezi sand, SiO_2 rises to nearly 90% in Luangwa sand, which contains a greater proportion of detritus recycled from Karoo siliciclastic strata. In sand of Lower Zambezi tributaries, SiO_2 mostly ranges between 70% and 80%. Composition is closest to the UCC for sand carried by the Lower Zambezi to the Indian Ocean, confirming its dominantly first-cycle provenance from midcrustal basement rocks (Garzanti et al. 2021*b*).

Chemical indices provide further clues. Because the addition of quartz grains profoundly affects the WIP, but not the CIA^*, the CIA^*/WIP ratio can be used to detangle the effects of weathering and recycling. This ratio reaches ≥100 in Uppermost Zambezi and Kwando sands consisting almost entirely of recycled Kalahari dune sand and decreases first to 30 ± 9 in Upper Zambezi sand above and below Victoria Falls and then drastically to 3.1 ± 0.7 in Upper Zambezi sand and silty sand upstream of Lake Kariba. The CIA^*/WIP ratio decreases further to 1.7 ± 0.3 in
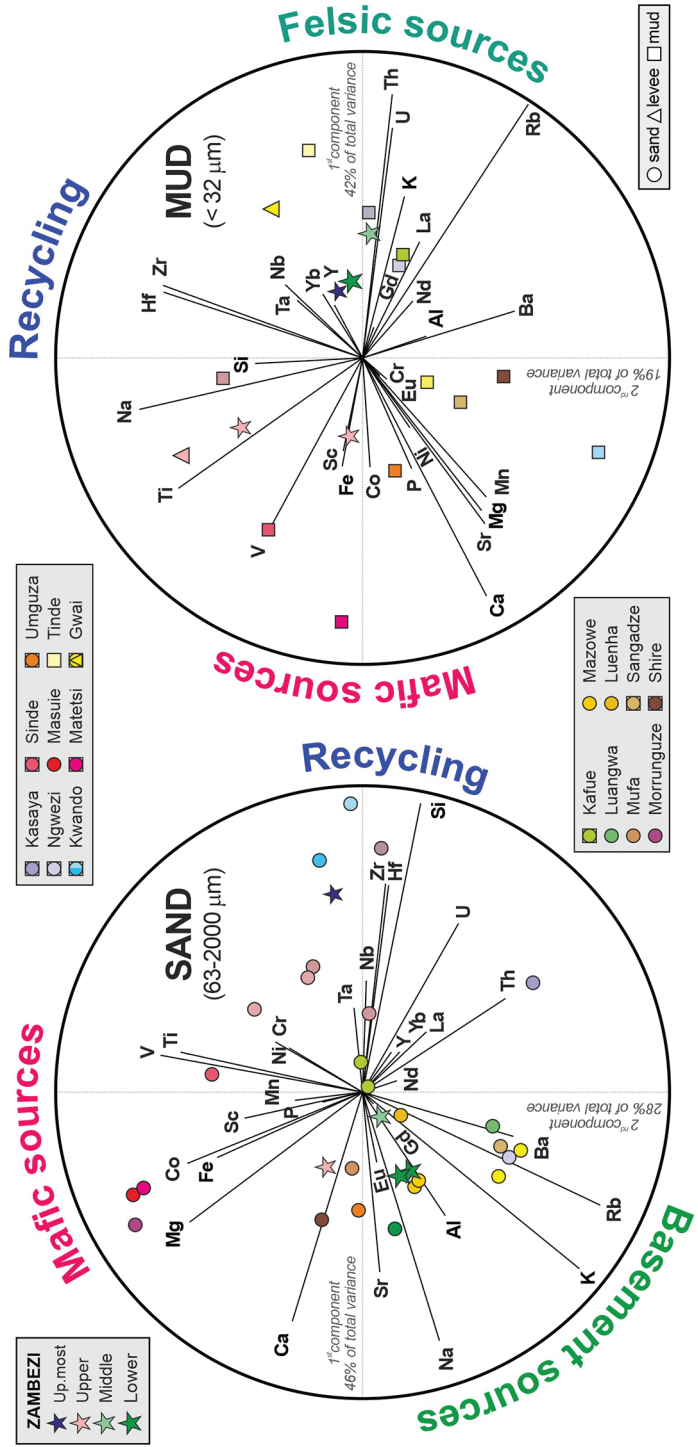
Figure 8. The biplots highlight the relationships among chemical elements in Zambezi sand and cohesive mud. Provenance control is most evident for sand. Ferromagnesian metals are enriched in basaltic or gabbroic detritus. Al, Na, Ca, K, Rb, Ba, and Eu hosted in feldspars are enriched in first-cycle detritus from midcrustal basements. Si, Zr, and Hf are enriched in sediment recycled from Kalahari dunes dominated by quartz and durable heavy minerals.

sands of Middle Zambezi tributaries and main stem and is lowest (0.9 ± 0.1) in sands of Lower Zambezi tributaries and main stem, further confirming their mostly first-cycle provenance.

Mud Geochemistry.   The geochemical composition of mud samples is more homogeneous. SiO_2 varies between 42% and 54%, being notably higher (68%) only for Tinde mud, reflecting recycling of siliciclastic Pan-African molasse. Kwando mud is markedly enriched in Ca, Sr, Mg, and Ba (fig. 4*B*), revealing contributions from calcrete and dolocrete soils (Shaw 2009; McFarlane et al. 2010). Fe, Ti, Sc, V, Co, and Cu are highest in Sinde mud and Mg in Matetsi mud (fig. 4*A*, 4*B*), largely derived from Karoo basalt. Lower Zambezi mud upstream of the delta is richest in Cr and Ni (fig. 4*H*), suggesting significant supply from mafic Proterozoic rocks, including the Tete gabbro-anorthosite.

Nd Isotope Geochemistry.   Although the $^{143}Nd/^{144}Nd$ composition of sediments is controlled by multiple factors, the provenance signal emerges clearly from data obtained from all analyzed size fractions—cohesive mud (<32 μm), very coarse silt (32–63 μm), and sand (63–2000 μm)—allowing a sharp distinction between sediments derived from mafic igneous rocks and old granitoid basements (fig. 9).

The least negative ε_{Nd} values characterize Morrunguze sand, largely derived from the upper Stenian Tete gabbro-anorthosite, and Sinde and Matetsi muds, partly derived from Lower Jurassic Karoo basalt (fig. 6). Mildly negative values were also obtained from Mufa sand, partly derived from Tete mafic rocks; from Shire sediments largely derived from mafic granulites of the Blantyre domain; and from Lower Zambezi silt collected at Tete and mostly derived from the southern Irumide Province (table 3).

At the other extreme, most negative ε_{Nd} values identify Gwai, Mazowe, and Luenha sands sourced from Archean gneiss of the Zimbabwe Craton. Markedly negative values also characterize mud in the upper catchments of the Zambezi and Gwai Rivers. The ε_{Nd} values becomes less negative as the Upper Zambezi rushes through the basaltic gorges downstream of Victoria Falls but much more negative as the lower Gwai cuts steeply across gneisses of the Dete-Kamativi Inlier. Strongly negative values also characterize Kafue and Luangwa sediments in the middle catchment, Sangadze sediment in the lowermost catchment, and Lower Zambezi sediment upstream of the delta.

Intrasample Variability.   The grain size–controlled intrasample variability of ε_{Nd} values is limited (average standard deviation: 1.6 ± 0.9).

The sand fraction (63–2000 μm) typically yields a more negative ε_{Nd} than the cohesive-mud fraction (<32 μm). The most negative ε_{Nd} values are obtained from the 32–63-μm size class of sand samples, representing the fine tail of the size distribution, where ultradense minerals, including LREE-rich monazite, concentrate because of the settling-equivalence effect (Rubey 1933). This is documented by La, Th, and Zr concentrations, respectively 7 ± 5, 9 ± 7, and 6 ± 3 times higher in the 32–63-μm size class than in the 63–2000-μm fraction of sand samples, with enrichment factors increasing sharply with sample grain size (correlation coefficient is 0.91; data from table A4). The opposite holds for the Lower Zambezi silt collected at Tete (fig. 6), where the 32–63-μm size class is part of the coarse tail of the size distribution, which is depleted in denser minerals and yields a less negative ε_{Nd} than both the <32-μm and 63–2000-μm fractions (table 3).

Intersample Variability.   Samples collected in nearby localities along the Kafue and Lower Zambezi Rivers confirm a tendency toward more negative ε_{Nd} values with increasing grain size. Strong grain-size control on ε_{Nd} has been recently documented in Congo Fan sediments, where it was ascribed to the more negative ε_{Nd} carried by multiply recycled quartz grains originally derived from older terrains on average (figs. 6 and 8 in Garzanti et al. 2021*a*). In recycled Congo Fan sediments, however, quartz and monazite account for similar amounts of Nd, quartz being 10^5 times more abundant in weight but monazite containing 10^5 times more Nd. In first-cycle Lower Zambezi sediments, instead, heavy minerals (including monazite) are an order of magnitude more abundant than in Congo sediments and are thus expected to dominate the REE budget (Totten et al. 2000). Among minerals frequently found in sediments, only monazite and allanite display very high LREE content, monazite being about three times richer in LREEs. In our sample set, monazite is about five times more abundant than allanite, which implies an order of magnitude greater contribution to the LREE sedimentary budget by monazite than by allanite. The tendency of ε_{Nd} values to become more negative in sand, and more markedly in the 32–63-μm size class of Middle and Lower Zambezi sand samples, thus suggests that ultradense monazite, strongly concentrated in the fine tail of the size distribution because of the settling-equivalence effect, carries an older (more negative) ε_{Nd} signal than other less dense and less durable minerals (e.g., allanite, titanite, apatite, epidote, and amphibole).

Model Ages.   The $T_{Nd,DM}$ model ages for the Zambezi main stem and tributaries mainly range
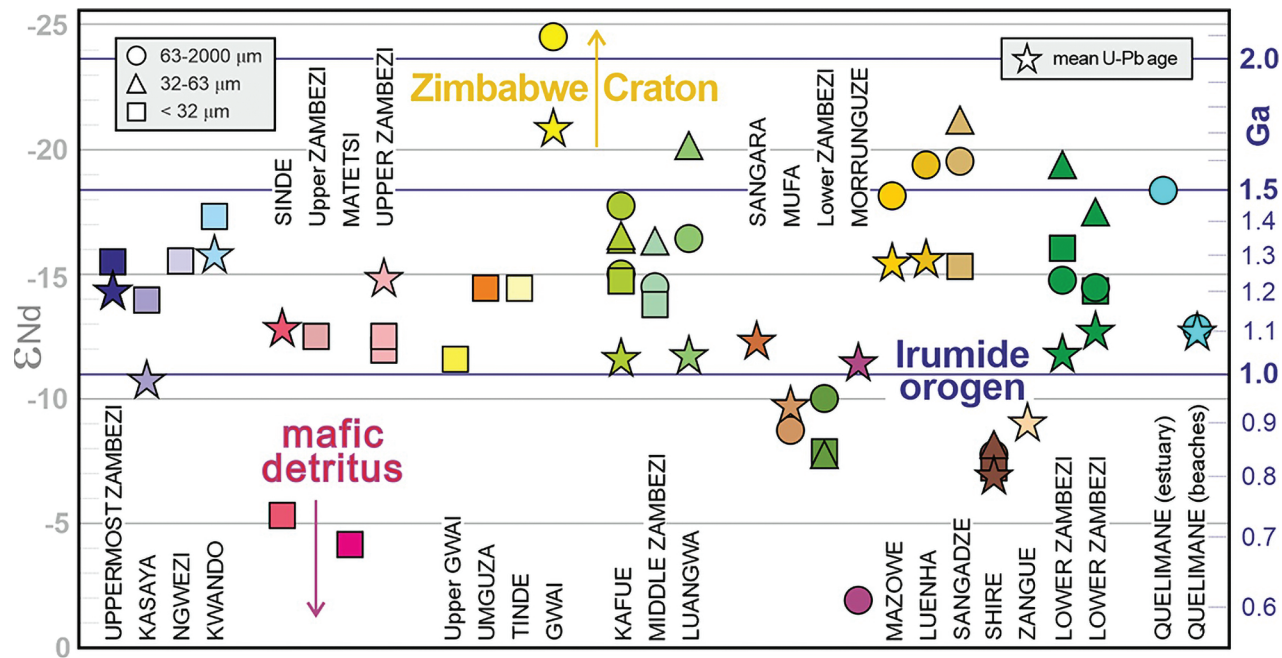
Figure 9.   Multiple controls on Nd isotope values. Most prominent are the effects of lithology (mafic detritus being least negative) and average age of source rocks (as highlighted by generally good correlation with U-Pb age of detrital zircon). Grain size–controlled intrasample variability is limited.

between 2.0 and 2.3 Ga (fig. 6). Mud partly derived from Karoo basalt yielded notably younger values (1.6 Ga for Sinde and 1.45 Ga for Matetsi), like all size fractions of Shire sediment largely derived from mafic granulites of the Blantyre domain (1.25–1.45 Ga). Morrunguze sand, largely derived from gabbroic rocks of the Tete domain, yielded the youngest value (1.16 Ga), whereas the oldest values (2.5–2.8 Ga) characterize the three rivers sourced in the Archean Zimbabwe Craton (Gwai, Mazowe, and Luenha; fig. 6).

Sm-Nd model ages depend on REE fractionation, being lower in samples containing LREE-rich minerals such as monazite or allanite and higher in samples containing middle-REE-rich minerals such as xenotime, titanite, or apatite (fig. 9 in Garzanti et al. 2021a). Because of the settling-equivalence effect, ultradense monazite grains occur only in the fine tail of the size distribution, which explains why the 32–63-μm size class of the cohesive Zambezi silt collected at Tete has a higher Sm/Nd ratio and thus yielded a notably higher Sm-Nd model age than the <32-μm fraction, despite its slightly lower ε_{Nd} (fig. 6). In the two Zambezi samples upstream of the delta, the 63–2000-μm fraction has lower LREE fractionation (higher Sm/Nd) than both the 32–63-μm and <32-μm fractions and thus yielded older Sm-Nd model ages than the <32-μm fraction, despite similar ε_{Nd} values, and almost the same Sm-Nd

model ages as the 32–63-μm size class, despite the latter yielding notably more negative ε_{Nd} (fig. 6).

Provenance Insights from Detrital Zircon Geochronology

Age spectra of detrital zircons enrich provenance information by providing insight into events of crustal growth in diverse source-rock domains (fig. 10). In the general case, however, these can be considered only "protosources" (Andersen et al. 2016, 2018). They represent the true sediment source only in the specific case of first-cycle detritus supplied directly from igneous or metamorphic basement (Dickinson et al. 2009). This introduces a further major uncertainty in zircon-based provenance analysis, because most sedimentary basins are fed with a mixture of recycled and first-cycle sediments in a proportion that can be evaluated only roughly from independent compositional data.

Petrographic, mineralogical, and geochemical data collectively concur to reveal that Uppermost Zambezi sand is dominantly recycled from Kalahari dune fields (Garzanti et al. 2014b). The Kwando River, in particular, drains entirely within the Kalahari Basin, whereas some first-cycle detritus is supplied by Zambian tributaries sourced in the Lufilian arc or the Choma-Kalomo Block. In sharp contrast, Lower Zambezi sand is mostly first cycle
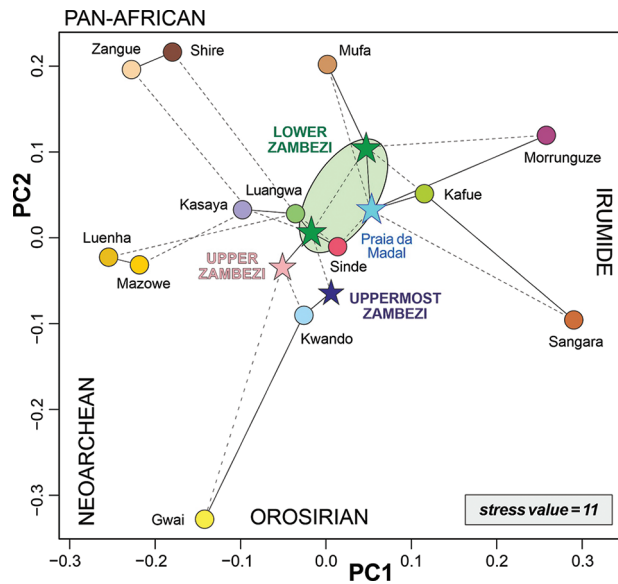
Figure 10. Multidimensional scaling map based on U-Pb zircon age spectra (green field defined by two Lower Zambezi samples upstream of the delta and Praia da Madal beach). Irumide ages are dominant in Sangara and Morrunguze sands. Pan-African ages prevail in Shire and Zangue sands. Neoarchean ages prevail in Gwai sand and are common in Luenha and Mazowe sands. Eburnean ages are common in Upper Zambezi, Kwando, and Gwai sands but never prevalent. A few Karoo ages occur in Kasaya and Sinde sands. Closest and second-closest neighbors are linked by solid and dashed lines, respectively. PC = principal component.

and derived from igneous and metamorphic Precambrian basements rejuvenated during Neogene southward propagation of the East African Rift.

Zircon Ages. Geochronological analysis indicates the Irumide and Pan-African crustal domains as the main protosources of zircon grains in rivers draining the northern Kalahari Plateau (fig. 7). Neoarchean ages ultimately derived from the Kasai Shield are common only for Kwando sand in the west. Paleoproterozoic grains ultimately derived from the Angola Block are more common in Kwando and Uppermost Zambezi sand than in eastern Zambian tributaries. Among these, Paleoproterozoic zircons are more common in Sinde sand sourced in the Choma-Kalomo Block, whereas Neoproterozoic zircons are much more abundant in Kasaya sand largely derived from the Lufilian Arc. The Irumide peak is invariably prominent. Zircon grains yielding Permian to Triassic Karoo ages constitute a minor population in Sinde sand but are lacking in Upper Zambezi sand downstream of the basaltic gorges, indicating that zircon occurs in tuffs inter-

layered within Karoo siliciclastic strata but not in the overlying Lower Jurassic basalt.

Despite extensive remobilization during the Pan-African orogeny (fig. 7 in Goscombe et al. 2020), the analyzed center of zircon grains in sand of northern (Kafue, Luangwa, Morrunguze) and western (Sangara, Mufa) tributaries to the Middle and upper Lower Zambezi yielded mostly or even exclusively Irumide ages (table 4). The dominant Irumide zircon age peak displayed by Kafue sand suggests that zircons sourced from the Neoproterozoic Lufilian Arc are retained in the Itezhi-Tezhi Reservoir and/or in the Kafue Flats and do not reach the lower gorge, where Irumide-aged zircons are derived largely from the Mpande Gneiss (~1.1. Ga; Hanson et al. 1994; fig. 6 in Goscombe et al. 2020).

Late Neoproterozoic ages are lacking in sand of the Morrunguze River, draining entirely within the southern Irumide Province, but are more abundant than Irumide ages in sand of the Shire and Zangue tributaries joining the Zambezi upstream of the delta (fig. 7). Archean zircons are common (24% ± 2%) in the Gwai, Mazowe, and Luenha Rivers, sourced in the Zimbabwe Craton. Gwai sand also carries ~30% of Paleoproterozoic zircons, largely derived from the Dete-Kamativi Inlier cut across in the lower course.

The multimodal age spectrum of Zambezi zircons eventually supplied to the delta and dragged by littoral currents to the northern Quelimane region indicates predominance of zircon grains derived directly or indirectly from the Irumide Belt, with subordinate late Neoproterozoic zircons mainly supplied by geological domains most severely remobilized during the Pan-African orogeny (fig. 7). Orosirian zircons are frequent, Neoarchean grains minor, and Permian–Triassic zircons rare (table 4).

A few Permian–Triassic zircons derived from Karoo volcanic or volcaniclastic layers are identified in Kasaya, Sinde, Gwai, Kafue, and Luangwa sands, but none were recorded from any Lower Zambezi tributary. Yet a few Permian–Triassic zircons occur in Lower Zambezi sand upstream of the delta, suggesting recycling of Karoo strata exposed in the Moatize-Minjova basin. Jurassic or Cretaceous ages are sporadically recorded. Among these, most significant are a couple of grains dated as ~120 Ma in the terminal tract of the Lower Zambezi, indicating provenance from igneous rocks emplaced during the incipient opening of the Mozambique Channel (König and Jokat 2010; Chanvry et al. 2018).

Zircon Fertility. The joint consideration of petrographic, mineralogical, and geochemical data sets offers not only a panorama of compositional

signatures but also useful information to evaluate the zircon fertility of sediment sources (e.g., diverse tributary catchments in the Zambezi drainage system), which is required for a correct use of zircon age data in the calculation of provenance budgets. Ultradense zircon is invariably segregated in the fine tail of the size distribution of each sample deposited by a tractive current and can be strongly concentrated locally by selective entrainment processes (Garzanti et al. 2008, 2009). These issues may hamper the accuracy of fertility determinations based on mineralogical or geochemical data (Malusà et al. 2016).

In our sample set, sands from the upper part of the Zambezi catchment have a notably lower concentration of zirconium (Zr is 232 ppm in one trunk-river sample but otherwise invariably below the UCC standard and mostly in the 30–80-ppm range) than in the Middle and Lower Zambezi catchments (between 330 and 600 ppm in Kafue and Mufa samples, and also above the UCC standard for the Middle Zambezi, Luenha, and Shire samples). Zircon concentration, calculated by combining petrographic and heavy-mineral point-counting data (tables A6, A7), is markedly lower in the Uppermost to Upper Zambezi catchment (median of bulk sand in volume is 0.02%, with a maximum of 0.2%) than in the Middle to Lower Zambezi catchment (median is 0.16% and maximum 0.6% for Shire sand).

A most useful parameter to detect hydraulically controlled concentration of denser minerals is the weighted average density of terrigenous grains (in g/cm^3; the SRD [source-rock density] index of Garzanti and Andò 2007), which for each sample should be equal to the weighted average density of source rocks in the ideal absence of environmental bias. The SRD index of most sands in rivers on the Kalahari Plateau ranges between 2.65 and 2.68 (just a little higher than quartz density), increasing to 2.79 and to 2.90 for Masuie and Matetsi sands containing, respectively, 50% and 70% detritus from dense basaltic rocks. In the Middle to Lower Zambezi catchment, SRD mostly ranges between 2.7 and 2.8, which matches the expected density range for upper to middle crustal basement rocks (Garzanti et al. 2006). The finer-grained Kafue (SRD: 2.79) and Luenha (SRD: 2.78) sands are richest in elements preferentially hosted in ultradense minerals (fig. 4). Luenha sand has high LREE and Th contents and negative LOI but only moderately high Zr, indicating concentration of ultradense monazite and magnetite but only moderately high zircon content (0.16% of bulk sand in volume;

table A7). The higher SRD values observed for Shire (2.82) and Morrunguze (2.87) sands reflect contribution from high-grade and largely mafic basement rocks of the Blantyre and Tete domains (figs. 2 and 7 in Goscombe et al. 2020). Ultradense garnet, zircon, monazite, and opaque Fe-Ti-Cr oxides have been markedly concentrated by selective entrainment processes only in Lower Zambezi sample S5778 (SRD 3.34), a fluvial garnet placer not analyzed for either geochemistry or zircon geochronology.

Petrographic, heavy-mineral, and geochemical data converge to indicate that the zircon concentration in our samples provides a broadly reliable indication of zircon fertility in the corresponding catchments. Zircon fertilities are estimated to range from 0.02% for Kalahari dune sands to 0.2% for midcrustal basement rocks exposed in the Lower Zambezi catchment.

Provenance Budgets and Erosion Patterns

Provenance Budgets. In this section, independent calculations based on elemental geochemistry and Nd isotope and geochronological data are used to better constrain the rough provenance budget based on detrital modes presented in Garzanti et al. (2021b). Integrated compositional data indicate that Upper Zambezi sand and silty sand delivered to Lake Kariba consist of ≥80% recycled quartz-rich Kalahari dunes and 16% ± 4% largely basaltic volcanic detritus, the remaining ≤5% being derived from Precambrian basements exposed in Zambia and Zimbabwe. The age spectrum of zircon grains supplied by the Upper Zambezi to Lake Kariba is intermediate between those of Uppermost Zambezi and Kwando sands. These two river branches are thus revealed as the most prominent zircon sources, in a relative proportion that cannot be accurately determined because of the low and similar zircon concentration in their sands indicated by mineralogical and geochemical data (table 2).

Because sand generated in the Upper and Middle Zambezi catchments is trapped in Lakes Kariba and Cahora Bassa, all sand ultimately delivered to the delta (zircon grains included) is generated within the Lower Zambezi catchment. Petrographic and heavy-mineral data indicate contributions in similar proportions (ca. 30%–40% each) from the southern Irumide Province, drained upstream of the Luenha confluence, and the Mazowe-Luenha river system, sourced in the Zimbabwe Craton. The Umkondo Belt and the Karoo, Cretaceous, and Cenozoic extensional basins, drained by the Minjova,

Sangadze, and Zangue tributaries, contribute much of the rest (~20%), whereas supply from the Tete and Blantyre domains, drained respectively by the Morrunguze and Shire tributaries, is subordinate (≤10% each; Garzanti et al. 2021b).

New complementary information obtained from elemental geochemistry suggests that as much as 70% of Lower Zambezi sand may be supplied by the Mazowe-Luenha river system, with subordinate contribution from the main stem upstream of the Zambezi-Luenha confluence (20%–25%) and minor supply from the Morrunguze and Shire Rivers (<5% each) and other lowermost-course tributaries (~5%). Calculations based on ε_{Nd} values of sand (63–2000-μm fraction) confirm that most Lower Zambezi sand is generated in the Mazowe-Luenha catchment (55%–65%), with subordinate contributions from the main stem upstream of the Luenha confluence and other sources. The ε_{Nd} values of cohesive mud (<32-μm fraction) in the Lower Zambezi upstream of the delta are similar to or more negative than those for sand (table 3). This indicates that the contribution from the Mazowe-Luenha river system is certainly not lower, and is probably higher, for mud than for sand.

Forward-mixing calculations based on zircon age data suggest that at least half of the zircon grains are derived from the Irumide domain, that a quarter, at most, are generated in the Mazowe-Luenha catchment, and that a fifth, at most, are generated in the final part of the Zambezi drainage basin, with a minor contribution from the Shire River. Because mineralogical and geochemical data indicate a relatively high zircon fertility for the Shire catchment, all compositional information converges to indicate that the Shire River supplies only a very small part (<5%) of the sediment to the Zambezi Delta. This holds true also for mud, because the smectite/kaolinite ratio increases sharply downstream of the Lower Zambezi, whereas Shire mud contains abundant kaolinite and minor smectite (table 1). Minor sediment supply from the Shire River is explained by sequestration in Lake Malawi of all sediment generated in the upper catchment and by further sediment trapping in wetlands and artificial reservoirs downstream (Mzuza et al. 2019). This inference contrasts with the findings of Just et al. (2014, p. 191), who reckoned that the Shire River contributes ~28% of total Zambezi sediment load at present (~21% before construction of the Cahora Bassa Dam).

Weighing Up Information. Provenance budgets based on independent data sets and on diverse size fractions are not entirely consistent. Age spectra of detrital zircons point at predominant zircon supply from the Irumide domain exposed in the upper part of the Lower Zambezi catchment, with minor zircon contribution from the Zimbabwe Craton, drained by the Mazowe and Luenha Rivers. Instead, elemental geochemistry and Nd isotope data suggest that most Lower Zambezi sediment is generated in the Mazowe-Luenha catchment. Although the robustness of diverse sets of calculations is not easily evaluated, it notably increases if end-member signatures are well distinct, precisely determined, and have little variability dependent on grain size, weathering, or hydraulic sorting. Conversely, estimates obtained on a narrow grain-size window or, worse, on a rare mineral within a narrow grain-size window, are least likely to be representative and accurately extrapolated to the entire sediment flux (Vezzoli et al. 2016).

In the case of Lower Zambezi tributaries draining medium-/high-grade crystalline basements, sand petrography, heavy-mineral, and elemental geochemistry signatures show significant overlap and hydrodynamically controlled variability. Least robust are calculations based on zircon age spectra, because of the uncertainties involved in zircon fertility determinations. Nd isotope geochemistry suffers from a limited number of analyzed samples, but the end members are well distinct and precisely defined, all grain sizes have been considered, and grain size–dependent variability is limited (fig. 9). The change toward much more negative ε_{Nd} documented in all size fractions of Lower Zambezi sediments downstream of the Luenha confluence cannot be ascribed to Shire sediments—which yielded even less negative ε_{Nd} values for all size fractions (fig. 6)—but clearly indicates major sediment supply from the Mazowe-Luenha river system. Weighing up all obtained information, we conclude that up to two-thirds of the sediment reaching the Zambezi Delta at present is generated in the Mazowe-Luenha catchment, between a quarter and a third between Lake Cahora Bassa and the Zambezi-Luenha confluence, and the rest downstream, with a very limited supply (≤5%) from the Shire River.

Erosion Patterns. Because of a general lack of gauged sediment loads, Zambezi sediment fluxes are evaluated with large uncertainties of a full order of magnitude. Erosion patterns across the catchment can thus be only grossly determined. On the basis of available sediment concentration data and sediment transport models, two end-member domains can be distinguished by their contrasting geomorphological conditions and sediment-generation modality: the low-relief Kalahari Plateau largely covered by eolian

sand in headwater regions and the rugged igneous and metamorphic terranes extensively exposed between Victoria Falls and the Mozambican lowlands.

On the plateau, rivers with low channel steepness sluggishly flow for large tracts through wetlands, where sediment is sequestered rather than produced, as in the Barotse floodplain and Chobe marshes on the main stem or the Machili and Kafue Flats traversed by the Kasaya, Ngwezi, and Kafue tributaries. Because data on Kwando sediment load are, to the best of our knowledge, unavailable, information from the Okavango River, similarly draining entirely within the Kalahari Basin in Angola (Shaw and Thomas 1992; McCarthy et al. 2012), allows us to broadly constrain the annual sediment yield and erosion rate in the Kalahari Basin as 2 ± 2 tons/km^2 and 0.001 ± 0.001 mm, respectively. This is notably lower than estimates based on cosmogenic nuclides for the Uppermost Zambezi catchment, including Precambrian terranes in the north (16 ± 2 tons/km^2 and 0.006 ± 0.001 mm; Wittmann et al. 2020). Sediment yield increases by an order of magnitude where channel steepness reaches very high values, as in basaltic gorges downstream of Victoria Falls (40–90 tons/km^2; fig. 3 and Garzanti et al. 2021b, p. 356).

A similar sediment-generation pattern characterizes other rivers flowing on the Kalahari Plateau in the headwaters and plunging into bedrock gorges downstream. For the Gwai River, a provenance budget based on petrographic, heavy-mineral, and geochemical data on both fluvial bar and levee silty sands indicates that sediment yield and erosion rate are between 20 and 50 times higher in the lower course cutting steeply across the Dete-Kamativi Inlier of the Magondi Belt than in the upper course sourced in the Zimbabwe Craton and draining the Kalahari Basin. The same may hold true for the Kafue River, where much of the sediment is, however, trapped in the Kafue Flats and behind the Itezhi-Tezhi and Kafue Gorge Dams.

Annual yields of 150 ± 50 tons/km^2, corresponding to erosion rates of 0.06 ± 0.02 mm, were estimated for Middle and Lower Zambezi tributaries flowing steeply across basement rocks exposed in the Archean Zimbabwe Craton or the Proterozoic lrumide, Umkondo, and Zambezi Belts of southern Zambia, northeastern Zimbabwe, and western Mozambique, respectively (Bolton 1984; Ronco et al. 2010). Considering that the Lower Zambezi upstream of the Luenha confluence and the Mazowe-Luenha river system have similar catchment areas, our provenance budget implies sediment yields and erosion rates between 1.5 and 2.5 times higher in the latter. Extensive sediment

trapping in Lake Malawi upstream and across wetlands or behind dams downstream (Mzuza et al. 2019) prevents us from making considerations concerning erosion rates in the Shire catchment.

Weathering versus Recycling

Insights from Clay Minerals. Clay mineralogy is quite sensitive to weathering conditions. It has long been observed that kaolinite is abundant in hot humid regions where feldspar hydrolysis is intense, whereas smectite is common in warm regions with a dry season characterized by intense evaporation, and illite and chlorite dominate where chemical decomposition is minor (Chamley 1989; Velde 1995). In modern sediments, the ratio between kaolinite and illite + chlorite (Kao/(Ill + Chl)) may thus be used as a proxy for weathering intensity (Liu et al. 2007; He et al. 2020). Within our sample set, kaolinite is significant in all catchments and represents ~40% of the clay mineral assemblage in Uppermost Zambezi, Lower Zambezi (Tete sample), and Shire muds (fig. 3). The Kao/(Ill + Chl) ratio is >1 in Uppermost Zambezi, Kwando, Ngwezi, and upper Gwai muds generated on the Kalahari Plateau but <1 in Middle and Lower Zambezi tributaries downstream (table 1).

Insights from Mud and Sand Geochemistry. Geochemical indices have long been used as proxies for weathering intensity (e.g., Nesbitt and Young 1982; Price and Velbel 2003), although they may be even predominantly controlled by grain size (von Eynatten et al. 2012, 2016), provenance (Garzanti and Resentini 2016; Dinis et al. 2017), hydraulic sorting, or quartz addition by recycling (fig. 11). This is especially true for sand, and weathering conditions are thus better reflected in the geochemistry of mud (Dinis et al. 2020a).

A most reliable indicator of weathering intensity is $\alpha^{Al}Na$, which chiefly measures the progressive leaching of Na$^+$ from the plagioclase lattice. The $\alpha^{Al}Na$ value decreases quite regularly from the Uppermost Zambezi and Kwando Rivers (21–22 for mud, ≥ 4 for sand) to Victoria Falls (4.6 for mud, 2.1 ± 0.1 for sand) and the Middle and Lower Zambezi (4.6 ± 0.4 for mud, 1.2 ± 0.1 for sand). Other α^{Al} values, and consequently the CIA* and its several derivative indices, are more significantly affected by the mineralogy of sediment sources. Most evident is the anomaly of Kwando mud, which is notably enriched in Ca, Sr, Mg, and Ba derived from erosion of calcrete soils (fig. 11) and consequently yields very low corresponding α^{Al} indices (≤ 0.4). Masuie, Matetsi, and Morrunguze sediments largely derived from basaltic
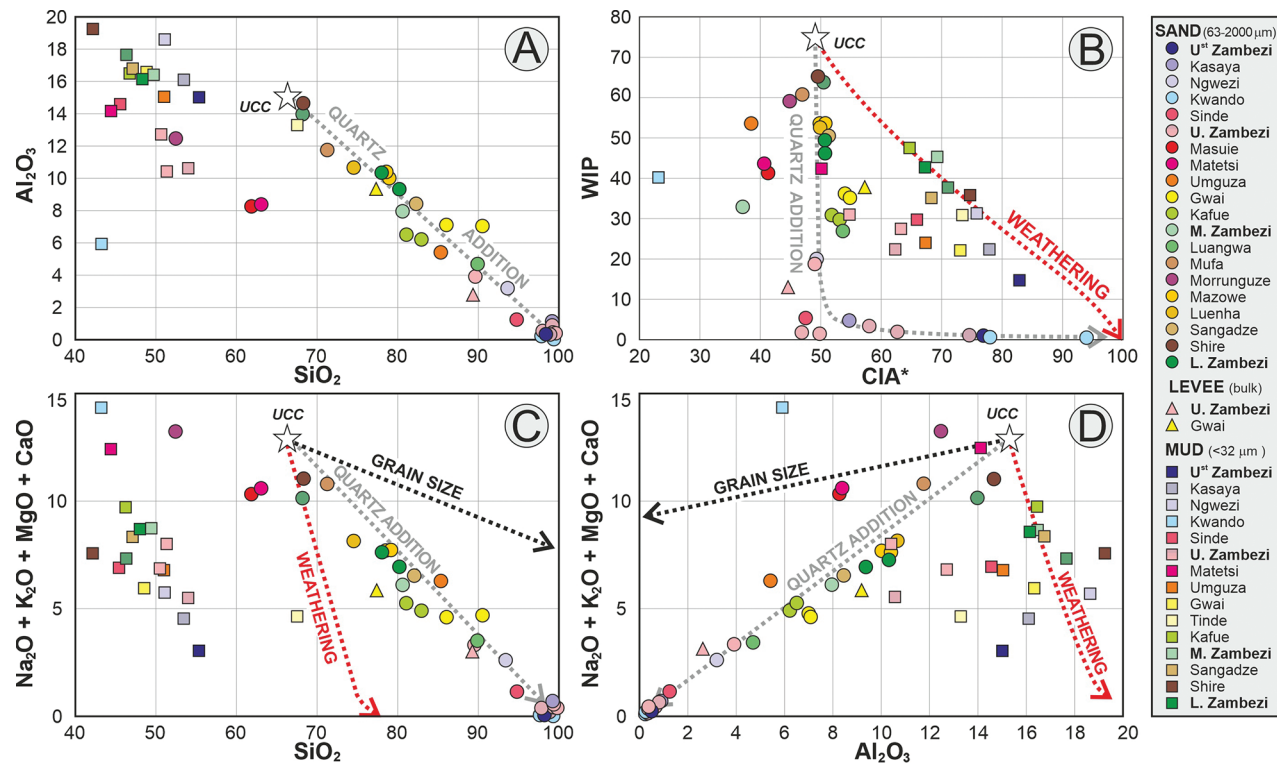
Figure 11. Discriminating the effects of weathering, recycling, and grain size from geochemical data. Theoretical trends are calculated starting from the UCC (upper continental crust) standard: the quartz-addition trend by progressively adding SiO_2, the weathering trend by progressively subtracting mobile metals relative to Si and Al. The grain-size trend is based on data from Alpine and Himalayan sediments (Garzanti et al. 2010a, 2011, 2012). In all four panels, sand follows the quartz-addition trend, reflecting recycling of Kalahari sands (Uppermost and Upper Zambezi catchments) or Karoo and older sandstones and metasandstones (Middle and Lower Zambezi catchments) to various degrees. Mud samples broadly follow the weathering trend. A, Samples plotting far below the regression line ($Al_2O_3 = -0.45SiO_2 + 45$) include Fe-rich Masuie and Matetsi sands from Karoo basalts and Kwando mud enriched in Ca, Sr, Mg, and Ba from calcrete soils. B, Uppermost (U^{st}) and Upper (U.) Zambezi muds plot below the weathering trend (low weathering index of Parker 1970 [WIP]), suggesting weathering signature inherited by recycling. CIA^* = chemical index of alteration. Middle (M.) and Lower (L.) Zambezi muds follow the theoretical trend, hinting at slightly increasing weathering intensity toward the coast. Calcrete erosion explains anomalously low CIA^* in Kwando mud. C, D, Cohesive muds collected upstream of Lake Kariba reflect quartz addition from Kalahari dunes (Uppermost Zambezi) or Neoproterozoic sandstones (Tinde).

or gabbroic rocks have high Mg and Ca contents and consequently low $\alpha^{Al}Mg$ and $\alpha^{Al}Ca$ (0.4–0.6). Conversely, sediments derived from gneissic basements are enriched in K and Rb largely hosted in K-feldspar and mica, which explains why $\alpha^{Al}K$ and $\alpha^{Al}Rb$ are <1 in several tributaries (e.g., Kasaya, Ngwezi, Gwai, Kafue, Luangwa, Mazowe, Luenha, and Sangadze). Sangadze sediments have the lowest plagioclase/K-feldspar ratio of all analyzed sands from the Lower Zambezi catchment and consequently yielded the highest $\alpha^{Al}Na$ in both mud and sand, and the lowest $\alpha^{Al}K$ and $\alpha^{Al}Rb$ in sand.

Insights from Detrital Minerals. Additional indications of weathering intensity can be inferred from the different durability of detrital minerals, although this path is fraught with pitfalls. An ex-

ample is the unfortunate use of the "mineralogical index of alteration" (MIA = quartz/(quartz + feldspar) × 100; Rieu et al. 2007), a misleading parameter not only long demonstrated to markedly increase with grain size (Odom et al. 1976) but also reaching maximum values equally in hyperhumid equatorial and hyperarid desert conditions (Garzanti et al. 2019; Pastore et al. 2021).

The differing chemical durability of heavy minerals is more reliably indicative (Bateman and Catt 2007). Particularly useful is the ratio between garnet (G) and other nesosilicates found in amphibole facies metapelites (SKAS = staurolite + kyanite + andalusite + sillimanite), which in sand of the Lower Zambezi catchment (G/(G + SKAS) = 72% ± 21%) is the same as in modern first-cycle sand derived

from metamorphic basements (G/(G + SKAS) = 70% ± 20%; Garzanti et al. 2010*b*). In contrast, the markedly anomalous low ratios (G/(G + SKAS) < 5%) that characterize sand in the Uppermost Zambezi catchment testify to an almost complete breakdown of garnet, a mineral that proves to be extremely vulnerable in equatorial soils (figs. 9*C*, 9*D* in Garzanti et al. 2013*a*) but very durable in a dry tropical climate (Garzanti et al. 2015). In recycled sand of the Kalahari Plateau, even zircon is selectively weathered out relative to quartz, as indicated by a zircon concentration lower by an order of magnitude than that of first-cycle sand shed by Precambrian basement rocks in the Middle to Lower Zambezi catchment. Zircon depletion is chiefly ascribed to breakdown of preferentially weathered, strongly metamict old grains (e.g., Balan et al. 2001; Resentini et al. 2020).

Corrosion Features. Direct evidence of chemical attack is provided by surficial dissolution textures on labile ferromagnesian minerals (Velbel 2007). This approach, however, has drawbacks: (1) surficial features tell us the state of what is preserved but nothing about how much was destroyed; (2) fresh and strongly weathered grains of the same detrital mineral commonly occur jointly (Van Loon and Mange 2007); and (3) slight degrees of corrosion might not be evaluated consistently by different operators. Only semiquantitative hints on the intensity of weathering can thus be obtained.

With this aim, the percentage of surficially etched grains and the degree of corrosion were recorded for over 4000 identified transparent heavy minerals, following the classification of Andò et al. (2012). In the Uppermost Zambezi main stem and tributaries, pyroxene, amphibole, epidote, staurolite, kyanite, and andalusite are all mainly unweathered, a minority of grains are corroded, and only a few pyroxene grains are deeply etched. In the Upper Zambezi main stem and tributaries, most grains are unweathered, but the percentage of corroded grains increases, and both pyroxene and amphibole may be deeply etched. In the Middle Zambezi main stem and tributaries, the percentage of corroded heavy minerals increases further, a larger percentage of pyroxene and amphibole grains are deeply etched, and also epidote, garnet, or kyanite may show deep etching. Similar features characterize the Lower Zambezi main stem and tributary sands, where epidote and garnet are even more extensively corroded.

Recycled Weathering Signatures. In the Uppermost Zambezi and Kwando Rivers, sand consists of quartz and durable heavy minerals, with very low G/(G + SKAS) ratios and CIA* > 75; mud contains abundant kaolinite, CIA* is >80, and $\alpha^{Al}Na$ is >20. Such compositional features, typical of sediment produced in a hot, humid equatorial climate, are at odds with the semiarid conditions of the Kalahari Plateau today. They testify to an intensity of chemical weathering that cannot occur in the present climatic regime but must have been inherited through multiple recycling from much wetter conditions of the past, most plausibly characterizing the subequatorial belt to the north (Garzanti et al. 2022). Diagenesis between sedimentary cycles contributed, too, but cannot account for all features (e.g., virtually complete selective breakdown of garnet). Weathered detritus from lower latitudes (~10°S), for instance, was supplied to the Kalahari Basin by the once-connected Chambeshi-Kafue river system, reaching the Uppermost Zambezi via the Machili Flats, as supported by fish lineages (Moore and Larkin 2001; Katongo et al. 2005).

Clay mineral assemblages in river muds across southern Africa are not kaolinite dominated, reflecting the limited efficiency of soil-forming processes and incomplete feldspar leaching under the present climatic conditions (Garzanti et al. 2014*a*). Kaolinite must thus be largely recycled from widespread relic lateritic paleosols and duricrusts (Partridge and Maud 1987; Dill 2007; Moore et al. 2009). Even in southern Malawi—where annual rainfall increases eastward from ~0.8 to 1.6 m at the foot of Mount Mulanje and 2.8 m at high elevation (3002 m above sea level)—kaolinite is mostly recycled by fluvial incision of peneplains of Cretaceous–Cenozoic age triggered by base-level lowering of the Shire River (Dill et al. 2005). This is corroborated by the great abundance of fresh feldspar in Shire sand (fig. 5*G* in Garzanti et al. 2021*b*), where inefficient plagioclase hydrolysis is testified to by undepleted Na and Ca ($\alpha^{Al}Na = \alpha^{Al}Ca = 1.0$).

All mineralogical and geochemical parameters, including Kao/(Ill + Chl), CIA*, and $\alpha^{Al}Na$, would consistently indicate that the weathering intensity recorded in modern river sediments decreases downstream the Zambezi River. Even when depurated from the physical effect of recycling (i.e., quartz addition), mud generated in the Uppermost Zambezi catchment appears to be more affected by weathering than Middle and Lower Zambezi mud (fig. 11). Such evidence, however, by no means implies that weathering on the dry Kalahari Plateau is at present more intense than that in the wetter Middle to Lower Zambezi catchment. Rather, this trend reflects mixing of distilled polycyclic detritus originally generated during some wetter stages of the past to the north of the Kalahari

dryland, with first-cycle detritus shed from Karoo basalts along the Upper Zambezi, followed by abrupt replacement—downstream of Lake Kariba first and of Lake Cahora Bassa next—by largely first-cycle detritus derived from Precambrian basements. Only in the Middle and Lower Zambezi, where detrital minerals are directly derived from basement rocks, do their surficial dissolution textures chiefly reflect present conditions of weathering. Together with trends displayed by cohesive mud (fig. 11*B*), these are the only features that document a slight increase in weathering intensity from the Middle to the Lower Zambezi catchment.

Conclusions

Any compositional parameter is invariably controlled by multiple physical and chemical processes that must be carefully evaluated before provenance and environmental information can be correctly detangled and understood. Diverse data sets obtained by a range of independent methods were thus integrated to constrain the many unknowns, reduce the number of potential alternative solutions, and increase the plausibility of our inferences. Following this rationale, we applied a spectrum of mineralogical, geochemical, and geochronological techniques to shed light on sedimentary processes active in the complex Zambezi big-river system.

In this study, such an approach allowed us to (1) characterize the composition of mud and sand generated in, and transported across, the Zambezi drainage basin; (2) monitor the evolution of compositional signals across a routing system rigidly segmented by both natural (tectonic depressions, lakes, wetlands) and anthropic (large reservoirs trapping all sediment generated upstream) factors; (3) make inferences on sediment yields and erosion rates even with a lack of gauged sediment fluxes; and (4) assess the intensity of weathering and the origin of weathering signatures (i.e., present vs. recycled) in diverse parts of the vast catchment.

The age spectra of detrital zircons reflect the major episodes of crustal growth in Precambrian southern Africa. Irumide ages are dominant in the Lower Zambezi and in most of its tributaries, excepting the Shire and the Zangue Rivers, where Pan-African ages prevail. Neoarchean ages characterize the Gwai, Mazowe, and Luenha Rivers, sourced in the Zimbabwe Craton. Eburnean ages are widely distributed but never prevail. Permian–Triassic (Karoo) ages are minor and Cretaceous ages rare.

Smectite is the most widespread clay mineral, dominant in mud from Karoo basalts, as in the warm and poorly drained Mozambican lowlands characterized by equatorial/winter-dry climate. Illite is prevalent locally (e.g., Kafue mud), and kaolinite is ubiquitous, reaching maximum abundance in both the uppermost and lower parts of the Zambezi catchment. Elemental geochemistry reflects overwhelming quartz addition by recycling of Kalahari dune sand in the Uppermost Zambezi, local supply from Lower Jurassic Karoo basalt in the Upper Zambezi, and chiefly first-cycle provenance from Precambrian basements in the Lower Zambezi.

The ε_{Nd} values range from mildly negative for sediment derived from Stenian gabbro, Tonian mafic granulite, and Jurassic basalt to strongly negative for sand derived from Neoarchean cratonic gneiss. The preferential concentration of ultradense monazite in the fine tail of the size distribution, owing to the settling-equivalence effect, controls the intrasample ε_{Nd} variability among cohesive-mud (<32 μm), very coarse silt (32–63 μm), and sand (63–2000 μm) fractions as well as deviations from the theoretical relationships between ε_{Nd} and $T_{Nd,DM}$ model ages, suggesting that durable monazite carries a more negative ε_{Nd} signal than other REE-bearing minerals (e.g., allanite, titanite, apatite, epidote, and amphibole).

Elemental and isotope geochemistry reveals that 55%–65% of mud and sand reaching the Zambezi Delta today, after the construction of the Kariba and Cahora Bassa Dams, is generated in the Mazowe-Luenha catchment. The contribution from Irumide terranes exposed upstream of the Luenha confluence is subordinate, and supply from the Shire River—the outlet of Lake Malawi—is minor. Although an accurate assessment of sediment yields and erosion rates is hampered by the lack of gauged sediment fluxes, annual estimates are lower by an order of magnitude on the Kalahari Plateau (10–20 tons/km^2 and ~0.005 mm) than in rugged terranes exposing Precambrian basements downstream (100–200 tons/km^2 and ~0.05 mm).

All mineralogical (garnet/SKAS, Kao/(Ill + Chl)) and geochemical (CIA*, α^{Al}Na) parameters consistently point to an intensity of chemical weathering on the Kalahari Plateau that cannot be related to modern dry-climate conditions. Chemical breakdown of virtually all minerals relative to quartz—including feldspars, garnet that is very labile in lateritic soils, and even zircon if strongly metamict—cannot occur in the Kalahari dryland, where kaolinite is recycled. Kaolinite is mostly produced by fluvial incision of relic Cretaceous–Cenozoic

paleosols even in the Shire catchment closer to the wetter Mozambican coast, where inefficient plagioclase hydrolysis is testified to by the dominance of fresh feldspars and undepleted Ca and Na. Indications of only slightly increasing weathering conditions in the Middle to Lower Zambezi catchment at present times are provided by mud geochemistry and surficial corrosion of pyroxene, amphibole, epidote, kyanite, and garnet.

SUPPLEMENTARY MATERIAL

Supplementary data associated with this article, available online, include information on sampling sites (table A1), together with data sets for clay mineralogy (table A2), elemental geochemistry (tables A3 and A4), Nd isotope geochemistry (table A5), bulk petrography (table A6), and heavy-minerals (table A7). Appendix A also contains the captions of appendix tables and further information on the rationale of forward-mixing calculations. The complete detrital zircon geochronology data set (U-Pb ages of zircon grains in the studied sand samples from the Zambezi River catchment; analyses made at the London Geochronology Centre, University College London) is contained in appendix B. A Google Earth map of sampling sites is also provided.

DATA AVAILABILITY

The mineralogical, geochemical, and geochronological data sets from this study are also available from the corresponding author upon request.

REFERENCES CITED

Aitchison, J., and Greenacre, M. 2002. Biplots of compositional data. J. R. Stat. Soc. C 51(4):375–392.

Alessio, B. L.; Collins, A. S.; Clark, C.; Glorie, S.; Siegfried, P. R.; and Taylor, R. 2019. Age, origin and palaeogeography of the southern Irumide Belt, Zambia. J. Geol. Soc. Lond. 176(3):505–516.

Allen, P. A. 2017. Sediment routing systems: the fate of sediment from source to sink. Cambridge, Cambridge University Press, 407 p.

Andersen, T.; Elburg, M. A.; van Niekerk, H. S.; and Ueckermann, H. 2018. Successive sedimentary recycling regimes in southwestern Gondwana: evidence from detrital zircons in Neoproterozoic to Cambrian sedimentary rocks in southern Africa. Earth-Sci. Rev. 181:43–60.

Andersen, T.; Kristoffersen, M.; and Elburg, M. A. 2016. How far can we trust provenance and crustal evolution information from detrital zircons? a South African case study. Gondwana Res. 34:129–148.

Andò, S.; Garzanti, E.; Padoan, M.; and Limonta, M. 2012. Corrosion of heavy minerals during weathering and diagenesis: a catalog for optical analysis. Sediment. Geol. 280:165–178.

Balan, E.; Neuville, D. R.; Trocellier, P.; Fritsch, E.; Muller, J.-P.; and Calas, G. 2001. Metamictization and chemical durability of detrital zircon. Am. Mineral. 86:1025–1033.

Banks, N. L.; Bardwell, K. A.; and Musiwa, S. 1995. Karoo Rift basins of the Luangwa Valley, Zambia. In Lambiase, J. J., ed. Hydrocarbon habitat in rift basins. Geol. Soc. Lond. Spec. Publ. 80:285–295.

Barrat, J. A.; Keller, F.; Amossé, J.; Taylor, R. N.; Nesbitt, R. W.; and Hirata, T. 1996. Determination of rare earth elements in sixteen silicate reference samples by ICP-MS after Tm addition and ion exchange separation. Geostand. Newsl. 20(1):133–139.

Barrat, J. A.; Zanda, B.; Moynier, F.; Bollinger, C.; Liorzou, C.; and Bayon, G. 2012. Geochemistry of CI chondrites: major and trace elements, and Cu and Zn isotopes: Geochim. Cosmochim. Acta 83:79–92.

Bateman, R. M., and Catt, J. A. 2007. Provenance and palaeoenvironmental interpretation of superficial deposits, with particular reference to post-depositional modification of heavy mineral assemblages. In Mange, M. A., and Wright, D. T., eds. Heavy minerals in use (Dev. Sedimentol., vol. 58). Amsterdam, Elsevier, p. 151–188.

Bayon, G.; German, C. R.; Boella, R. M.; Milton, J. A.; Taylor, R. N.; and Nesbitt, R. W. 2002. An improved method for extracting marine sediment fractions and its application to Sr and Nd isotopic analysis. Chem. Geol. 187:179–199.

Beilfuss, R., and dos Santos, D. 2001. Patterns of hydrological change in the Zambezi delta, Mozambique.

Program for the Sustainable Management of the Cahora Bassa Dam and the Lower Zambezi Valley Working Paper no. 2. Baraboo, WI, Int. Crane Found., 159 p.

Bolton, P. 1984. Sediment deposition in major reservoirs in the Zambezi Basin. *In* Walling, D. E.; Foster, S. S. D.; and Wurzel, P., eds. Challenges in African hydrology and water resources: proceedings of the Harare Symposium, July 1984. Int. Assoc. Hydrol. Sci. Publ. 144:559–567.

Bouvier, A.; Vervoort, J. D.; and Patchett, P. J. 2008. The Lu-Hf and Sm-Nd isotopic composition of CHUR: constraints from unequilibrated chondrites and implications for the bulk composition of terrestrial planets. Earth Planet. Sci. Lett. 273:48–57.

Bulambo, M.; De Waele, B.; Kokonyangi, J.; Johnson, S. P.; Kampunzu, A. B.; and Tembo, F. 2006. SHRIMP zircon U-Pb geochronology and geochemistry of the Choma-Kalomo Block granitoids (Zambia): geological implications. *In* Colloquium of African Geology, 21st (Maputo, Mozambique), Abstr., p. 26–27.

Burrough, S. L.; Thomas, D. S.; and Bailey, R. M. 2009. Mega-Lake in the Kalahari: a Late Pleistocene record of the Palaeolake Makgadikgadi system. Quat. Sci. Rev. 28(15–16):1392–1411.

Burrough, S. L.; Thomas, D. S. G.; and Barham, L. S. 2019. Implications of a new chronology for the interpretation of the Middle and Later Stone Age of the upper Zambezi Valley. J. Archaeol. Sci. Rep. 23:376–389.

Butt, A. J., and Gould, K. 2018. 3D source-rock modelling in frontier basins: a case study from the Zambezi Delta Depression. Pet. Geosci. 24(3):277–286.

Calamita, E.; Schmid, M.; Kunz, M.; Ndebele-Murisa, M. R.; Magadza, C. H.; Nyambe, I.; and Wehrli, B. 2019. Sixty years since the creation of Lake Kariba: thermal and oxygen dynamics in the riverine and lacustrine sub-basins. PloS ONE 14(11):e0224679. https://doi.org/10.1371/journal.pone.0224679.

Catuneanu, O.; Wopfner, H.; Eriksson, P. G.; Cairncross, B.; Rubidge, B. S.; Smith, R. M. H.; and Hancox, P. J. 2005. The Karoo basins of south-central Africa. J. Afr. Earth Sci. 43(1–3):211–253.

Chamley, H. 1989. Clay mineralogy. Berlin, Springer, 623 p.

Chanvry, E.; Andò, S.; Garzanti, E.; Guillocheau, F.; Dall'Asta, M.; Beaufort, D.; and Patrier, P. 2018. Impact of hinterland evolution in mineralogy of clastics sediments: first results from mineralogical analysis focus on the Zambezi system during Meso-Cenozoic times. European Geosciences Union General Assembly Conference. Geophys. Res. Abstr. 20:EGU2018-18077.

Comas, M., and Thió-Henestrosa, S. 2011. CoDaPack 2.0: a stand-alone, multi-platform compositional software. *In* Egozcue, J. J.; Tolosana-Delgado, R.; and Ortego, M. I. eds. International Workshop on Compositional Data Analysis, 4th (Girona, Spain), Proc., 10 p.

Cox, K. G. 1989. The role of mantle plumes in the development of continental drainage patterns. Nature 342(6252):873–877.

Daly, M. C.; Green, P.; Watts, A. B.; Davies, O.; Chibesakunda, F.; and Walker, R. 2020. Tectonics and landscape of the Central African Plateau and their implications for a propagating Southwestern Rift in Africa. Geochem. Geophys. Geosyst. 21(6):e2019GC008746. https://doi.org/10.1029/2019GC008746.

Davies, B. R.; Beilfuss, R. D.; and Thoms, M. C. 2000. Cahora Bassa retrospective, 1974–1997: effects of flow regulation on the Lower Zambezi River. Int. Ver. Theor. Angew. Limnol. Verh. 27(4):2149–2157.

De Carvalho, H.; Tassinari, C.; Alves, P. H.; Guimarães, F.; and Simões, M. C. 2000. Geochronological review of the Precambrian in western Angola: links with Brazil. J. Afr. Earth Sci. 31(2):383–402.

De Paolo, D. J. 1981. Neodymium isotopes in the Colorado Front Range and crust-mantle evolution in the Proterozoic. Nature 291(5812):193–196.

Derricourt, R. M. 1976. Regression rate of the Victoria Falls and the Batoka Gorge. Nature 264:23–25.

De Waele, B.; Fitzsimons, I. C. W.; Wingate, M. T. D.; Tembo, F.; Mapani, B.; and Belousova, E. A. 2009. The geochronological framework of the Irumide Belt: a prolonged crustal history along the margin of the Bangweulu Craton. Am. J. Sci. 309(2):132–187.

De Waele, B.; Kampunzu, A. B.; Mapani, B. S. E.; and Tembo, F. 2006. The Mesoproterozoic Irumide Belt of Zambia. J. Afr. Earth Sci. 46(1–2):36–70.

De Waele, B.; Wingate, M. T.; Fitzsimons, I. C.; and Mapani, B. S. 2003. Untying the Kibaran knot: a reassessment of Mesoproterozoic correlations in southern Africa based on SHRIMP U-Pb data from the Irumide Belt. Geology 31(6):509–512.

Dickinson, W. R.; Lawton, T. F.; and Gehrels, G. E. 2009. Recycling detrital zircons: a case study from the Cretaceous Bisbee Group of southern Arizona. Geology 37(6):503–506.

Dill, H. G. 2007. A review of mineral resources in Malawi: with special reference to aluminium variation in mineral deposits. J. Afr. Earth Sci. 47(3):153–173.

Dill, H. G.; Ludwig, R. R.; Kathewera, A.; and Mwenelupembe, J. 2005. A lithofacies terrain model for the Blantyre region: implications for the interpretation of palaeosavanna depositional systems and for environmental geology and economic geology in southern Malawi. J. Afr. Earth Sci. 41(5):341–393.

Dinis, P.; Garzanti, E.; Hahn, A.; Vermeesch, P.; and Cabral-Pinto, M. 2020*a*. Weathering indices as climate proxies. A step forward based on Congo and SW African river muds. Earth-Sci. Rev. 201:103039.

Dinis, P.; Garzanti, E.; Vermeesch, P.; and Huvi, J. 2017. Climatic zonation and weathering control on sediment composition (Angola). Chem. Geol. 467:110–121.

Dinis, P.; Sequeira, M.; Tavares, A. O.; Carvalho, J.; Castilho, A.; and Cabral-Pinto, M. 2020*b*. Post-wildfire denudation assessed from compositional features of river sediments (central Portugal). Appl. Clay Sci. 193:105675.

Dirks, P. H. G. M.; Blenkinsop, T. G.; and Jelsma, H. A. 2009. The geological evolution of Africa. *In* De Vivo, B.; Grasemann, B.; and Stüwe, K., eds. Geology, vol. 4.

Paris, EOLSS (Encyclopedia of Life Support Systems), p. 230–251.

Ebinger, C. E., and Scholz, C. A. 2012. Continental rift basins: the East African perspective. *In* Busby, C., and Azor, A., eds. Tectonics of sedimentary basins: recent advances. Oxford, Wiley-Blackwell, p. 185–208.

Eglinger, A.; Vanderhaeghe, O.; André-Mayer, A. S.; Goncalves, P.; Zeh, A.; Durand, C.; and Deloule, E. 2016. Tectono-metamorphic evolution of the internal zone of the Pan-African Lufilian orogenic belt (Zambia): implications for crustal reworking and synorogenic uranium mineralizations. Lithos 240–243:167–188.

ERM (Environmental Resources Management). 2011. Riversdale's Zambezi River Barging Project, Zambezi River, Mozambique: final environmental and social impact assessment report. Johannesburg, ERM, 335 p.

Fernandes, P.; Cogné, N.; Chew, D. M.; Rodrigues, B.; Jorge, R. C. G. S.; Marques, J.; Jamal, D.; and Vasconcelos, L. 2015. The thermal history of the Karoo Moatize-Minjova Basin, Tete Province, Mozambique: an integrated vitrinite reflectance and apatite fission track thermochronology study. J. Afr. Earth Sci. 112:55–72.

FFEM (Fonds Français pour l'Environnement Mondial). 2005. Pollution monitoring and management on the Zambezi River: final report. Lusaka, Zambia, FFEM.

Frimmel, H. E.; Basei, M. S.; and Gaucher, C. 2011. Neoproterozoic geodynamic evolution of SW-Gondwana: a southern African perspective. Int. J. Earth Sci. 100:323–354.

Fritz, H.; Abdelsalam, M.; Ali, K. A.; Bingen, B.; Collins, A. S.; Fowler, A. R.; Ghebreab, W.; et al. 2013. Orogen styles in the East African orogen: a review of the Neoproterozoic to Cambrian tectonic evolution. J. Afr. Earth Sci. 86:65–106.

Gabriel, K. R. 1971. The biplot graphic display of matrices with application to principal component analysis. Biometrika 58:453–467.

Gaillardet, J.; Dupré, B.; and Allègre, C. J. 1999. Geochemistry of large river suspended sediments: silicate weathering or recycling tracer? Geochim. Cosmochim. Acta 63:4037–4051.

Garzanti, E., and Andò, S. 2007. Heavy-mineral concentration in modern sands: implications for provenance interpretation. *In* Mange, M. A., and Wright, D. T., eds. Heavy minerals in use (Dev. Sedimentol., vol. 58). Amsterdam, Elsevier, p. 517–545.

Garzanti, E.; Andò, S.; France-Lanord, C.; Censi, P.; Vignola, P.; Galy, V.; and Lupker, M. 2011. Mineralogical and chemical variability of fluvial sediments: 2. Suspended-load silt (Ganga-Brahmaputra, Bangladesh). Earth Planet. Sci. Lett. 302(1–2):107–120.

Garzanti, E.; Andò, S.; France-Lanord, C.; Vezzoli, G.; Censi, P.; Galy, V.; and Najman, Y. 2010a. Mineralogical and chemical variability of fluvial sediments: 1. Bedload sand (Ganga-Brahmaputra, Bangladesh). Earth Planet. Sci. Lett. 299(3–4):368–381.

Garzanti, E.; Andò, S.; and Vezzoli, G. 2006. The continental crust as a source of sand (Southern Alps cross section, northern Italy). J. Geol. 114:533–554.

———. 2008. Settling equivalence of detrital minerals and grain-size dependence of sediment composition. Earth Planet. Sci. Lett. 273(1–2):138–151.

———. 2009. Grain-size dependence of sediment composition and environmental bias in provenance studies. Earth Planet. Sci. Lett. 277:422–432.

Garzanti, E.; Bayon, G.; Dennielou, B.; Barbarano, M.; Limonta, M.; and Vezzoli, G. 2021a. The Congo deep-sea fan: mineralogical, REE, and Nd-isotope variability in quartzose passive-margin sand. J. Sediment. Res. 91(5):433–450.

Garzanti, E.; Padoan, M.; Andò, S.; Resentini, A.; Vezzoli, G.; and Lustrino, M. 2013a. Weathering and relative durability of detrital minerals in equatorial climate: sand petrology and geochemistry in the East African Rift. J. Geol. 121:547–580.

Garzanti, E.; Padoan, M.; Setti, M.; López-Galindo, A.; and Villa, I. M. 2014a. Provenance versus weathering control on the composition of tropical river mud (southern Africa). Chem. Geol. 366:61–74.

Garzanti, E.; Padoan, M.; Setti, M.; Peruta, L.; Najman, Y.; and Villa, I. M. 2013b. Weathering geochemistry and Sr-Nd fingerprints of equatorial upper Nile and Congo muds. Geochem. Geophys. Geosyst. 14:292–316.

Garzanti, E.; Pastore, G.; Resentini, A.; Vezzoli, G.; Vermeesch, P.; Ncube, L.; Van Niekerk, H.-G.; Jouet, G.; and Dall'Asta, M. 2021b. The segmented Zambezi sedimentary system from source to sink: 1. Sand petrology and heavy minerals. J. Geol. 129(4):343–369. https://doi.org/10.1086/715792.

Garzanti, E.; Pastore, G.; Stone, A.; Vainer, S.; Vermeesch, P.; and Resentini, A. 2022. Provenance of Kalahari sand: paleoweathering and recycling in a linked fluvial-aeolian system. Earth-Sci. Rev. 224:103867. https://doi.org/10.1016/j.earscirev.2021.103867.

Garzanti, E., and Resentini, A. 2016. Provenance control on chemical indices of weathering (Taiwan river sands). Sediment. Geol. 336:81–95.

Garzanti, E.; Resentini, A.; Andò, S.; Vezzoli, G.; Pereira, A.; and Vermeesch, P. 2015. Physical controls on sand composition and relative durability of detrital minerals during ultra-long-distance littoral and aeolian transport (Namibia and southern Angola). Sedimentology 62(4):971–996.

Garzanti, E.; Resentini, A.; Vezzoli, G.; Andò, S.; Malusà, M.; and Padoan, M. 2012. Forward compositional modelling of Alpine orogenic sediments. Sediment. Geol. 280:149–164.

Garzanti, E.; Resentini, A.; Vezzoli, G.; Andò, S.; Malusà, M. G.; Padoan, M.; and Paparella, P. 2010b. Detrital fingerprints of fossil continental-subduction zones (axial belt provenance, European Alps). J. Geol. 118:341–362.

Garzanti, E.; Vermeesch, P.; Padoan, M.; Resentini, A.; Vezzoli, G.; and Andò, S. 2014b. Provenance of passive-margin sand (southern Africa). J. Geol. 122:17–42.

Garzanti, E.; Vermeesch, P.; Rittner, M.; and Simmons, M. 2018. The zircon story of the Nile: time-structure maps of source rocks and discontinuous propagation of detrital signals. Basin Res. 30:1098–1117.

Garzanti, E.; Vermeesch, P.; Vezzoli, G.; Andò, S.; Botti, E.; Limonta, M.; Dinis, P.; et al. 2019. Congo River sand and the equatorial quartz factory. Earth-Sci. Rev. 197:102918. https://doi.org/10.1016/j.earscirev.2019.102918.

Glynn, S. M.; Master, S.; Frei, D.; and Wiedenbeck, M. 2020. U-Pb zircon geochronology of the Dete-Kamativi Inlier, NW Zimbabwe, with implications for the western margin of the Archaean Zimbabwe Craton. Precambrian Res. 346:105824.

Glynn, S. M.; Master, S.; Wiedenbeck, M.; Davis, D. W.; Kramers, J. D.; Belyanin, G. A.; Frei, D.; and Oberthür, T. 2017. The Proterozoic Choma-Kalomo Block, SE Zambia: exotic terrane or a reworked segment of the Zimbabwe Craton? Precambrian Res. 298:421–438.

Goscombe, B.; Foster, D. A.; Gray, D.; and Wade, B. 2020. Assembly of central Gondwana along the Zambezi Belt: metamorphic response and basement reactivation during the Kuunga orogeny. Gondwana Res. 80:410–465.

Greber, N. D.; Davies, J. H.; Gaynor, S. P.; Jourdan, F.; Bertrand, H.; and Schaltegger, U. 2020. New high precision U-Pb ages and Hf isotope data from the Karoo large igneous province; implications for pulsed magmatism and early Toarcian environmental perturbations. Results Geochem. 1:100005.

Griffin, W. L.; Powell, W. J.; Pearson, N. J.; and O'Reilly, S. Y. 2008. GLITTER: data reduction software for laser ablation ICP-MS. *In* Sylvester, P., ed. Laser ablation-ICP-MS in the earth sciences: current practices and outstanding issues. Mineral. Assoc. Can. Short Course 40:204–207.

Gumbricht, T.; McCarthy, T. S.; and Merry, C. L. 2001. The topography of the Okavango Delta, Botswana, and its tectonic and sedimentological implications. S. Afr. J. Geol. 104(3):243–264.

Haddon, I. G., and McCarthy, T. S. 2005. The Mesozoic–Cenozoic interior sag basins of Central Africa: the Late-Cretaceous–Cenozoic Kalahari and Okavango basins. J. Afr. Earth Sci. 43:316–333.

Hanson, R. E. 2003. Proterozoic geochronology and tectonic evolution of southern Africa. *In* Yoshida, M.; Windley, B. F.; and Dasgupta, S., eds. Proterozoic East Gondwana: supercontinent assembly and breakup. Geol. Soc. Lond. Spec. Publ. 206:427–463.

Hanson, R. E.; Harmer, R. E.; Blenkinsop, T. G.; Bullen, D. S.; Dalziel, I. W. D.; Gose, W. A.; Hall, R. P.; et al. 2006. Mesoproterozoic intraplate magmatism in the Kalahari Craton: a review. J. Afr. Earth Sci. 46(1–2):141–167.

Hanson, R. E.; Wilson, T. J.; and Munyanyiwa, H. 1994. Geologic evolution of the Neoproterozoic Zambezi orogenic belt in Zambia. J. Afr. Earth Sci. 18(2):135–150.

Hargrove, U. S.; Hanson, R. E.; Martin, M. W.; and Munyanyiwa, H. 2003. Tectonic evolution of the Zambezi orogenic belt: geochronological, structural, and petrological constraints from northern Zimbabwe. Precambrian Res. 123(2–4):159–186.

Hay, W. W. 1998. Detrital sediment fluxes from continents to oceans. Chem. Geol. 145:287–323.

He, J.; Garzanti, E.; Dinis, P.; Yang, S.; and Wang, H. 2020. Provenance versus weathering control on sediment composition in tropical monsoonal climate (South China) - 1. Geochemistry and clay mineralogy. Chem. Geol. 558:119860.

Hinderer, M. 2012. From gullies to mountain belts: a review of sediment budgets at various scales. Sediment. Geol. 280:21–59.

Howard, E., and Washington, R. 2019. Drylines in southern Africa: rediscovering the Congo Air Boundary. J. Climate 32:8223–8242.

Jackson, S. E.; Pearson, N. J.; Griffin, W. L.; and Belousova, E. A. 2004. The application of laser ablation-inductively coupled plasma-mass spectrometry to in situ U-Pb zircon geochronology. Chem. Geol. 211:47–69.

Jacobs, J.; Pisarevsky, S.; Thomas, R. J.; and Becker, T. 2008. The Kalahari Craton during the assembly and dispersal of Rodinia. Precambrian Res. 160:142–158.

Jelsma, H. A., and Dirks, P. H. G. M. 2002. Neoarchaean tectonic evolution of the Zimbabwe Craton. *In* Fowler, C. M. R.; Ebinger, C. J.; and Hawkesworth, C. J., eds. The early Earth: physical, chemical, and biological development. Geol. Soc. Lond. Spec. Publ. 199:183–211.

Jelsma, H. A.; McCourt, S.; Perritt, S. H.; and Armstrong, R. A. 2018. The geology and evolution of the Angolan Shield, Congo Craton. *In* Siegesmund, S.; Basei, M.; Oyhantçabal, P.; and Oriolo, S., eds. Geology of Southwest Gondwana (Regional Geol. Rev.). Cham, Springer, p. 217–239. https://doi.org/10.1007/978-3-319-68920-3_9.

John, T.; Schenk, V.; Haase, K.; Scherer, E.; and Tembo, F. 2003. Evidence for a Neoproterozoic ocean in south-central Africa from mid-ocean-ridge-type geochemical signatures and pressure-temperature estimates of Zambian eclogites. Geology 31:243–246.

John, T.; Schenk, V.; Mezger, K.; and Tembo, F. 2004. Timing and *PT* evolution of whiteschist metamorphism in the Lufilian Arc–Zambezi Belt orogen (Zambia): implications for the assembly of Gondwana. J. Geol. 112(1):71–90.

Johnson, M. R. 1991. Sandstone petrography, provenance, and plate tectonic setting in Gondwana context of the southeastern Cape-Karoo Basin. S. Afr. J. Geol. 94:137–154.

Johnson, M. R.; Van Vuuren, C. J.; Hegenberger, W. F.; Key, R.; and Show, U. 1996. Stratigraphy of the Karoo Supergroup in southern Africa: an overview. J. Afr. Earth Sci. 23(1):3–15.

Johnsson, M. J. 1993. The system controlling the composition of clastic sediments. *In* Johnsson, M. J., and Basu, A. eds. Processes controlling the composition of clastic sediments. Geol. Soc. Am. Spec. Pap. 284:1–19.

Jury, M. 2010. Climate and weather factors modulating river flows in southern Angola. Int. J. Climatol. 30:901–908.

Just, J.; Schefuß, E.; Kuhlmann, H.; Stuut, J.-B. W.; and Pätzold, J. 2014. Climate induced sub-basin source-area

shifts of Zambezi River sediments over the past 17 ka. Palaeogeogr. Palaeoclimatol. Palaeoecol. 410:190–199.

Kahle, M.; Kleber, M.; and Jahn, R. 2002. Review of XRD-based quantitative analyses of clay minerals in soils: the suitability of mineral intensity factors. Geoderma 109:191–205.

Kampunzu, A. B., and Cailteux, J. 1999. Tectonic evolution of the Lufilian Arc (Central Africa Copper Belt) during Neoproterozoic Pan African orogenesis. Gondwana Res. 2(3):401–421.

Katongo, C.; Koblmüller, S.; Duftner, N.; Makasa, L.; and Sturmbauer, C. 2005. Phylogeography and speciation in the *Pseudocrenilabrus philander* species complex in Zambian rivers. *In* Segers, H., and Martens, K. eds. Aquatic biodiversity II (Dev. Hydrobiol., vol. 180). Dordrecht, Springer, p. 221–233.

Key, R. M.; Cotterill, F. P. D.; and Moore, A. E. 2015. The Zambezi River: an archive of tectonic events linked to the amalgamation and disruption of Gondwana and subsequent evolution of the African plate. S. Afr. J. Geol. 118(4):425–438.

König, M., and Jokat, W. 2010. Advanced insights into magmatism and volcanism of the Mozambique Ridge and Mozambique Basin in the view of new potential field data. Geophys. J. Int. 180(1):158–180.

Kottek, M.; Grieser, J.; Beck, C.; Rudolf, B.; and Rubel, F. 2006. World map of the Köppen-Geiger climate classification updated. Meteorol. Z. 15:259–263.

Kruskal, J. B., and Wish, M. 1978. Multidimensional scaling. Sage Univ. Paper no. 07-011. Newbury Park, CA, Sage, 92 p.

Kunz, M. J.; Anselmetti, F. S.; Wüest, A.; Wehrli, B.; Vollenweider, A.; Thüring, S.; and Senn, D. B. 2011. Sediment accumulation and carbon, nitrogen, and phosphorus deposition in the large tropical reservoir Lake Kariba (Zambia/Zimbabwe). J. Geophys. Res. Biogeosci. 116(G3):G03003. https://doi.org/10.1029/2010JG001538.

Kusky, T. M. 1998. Tectonic setting and terrane accretion of the Archean Zimbabwe craton. Geology 26:163–166.

Lanci, L.; Tohver, E.; Wilson, A.; and Flint, S. 2013. Upper Permian magnetic stratigraphy of the lower Beaufort group, Karoo basin. Earth Planet. Sci. Lett. 375:123–134.

Liu, Z.; Zhao, Y.; Li, J.; and Colin, C. 2007. Late Quaternary clay minerals off Middle Vietnam in the western South China Sea: implications for source analysis and East Asian monsoon evolution. Sci. China Ser. D Earth Sci. 50(11):1674–1684.

Ludwig, K. R. 1998. On the treatment of concordant uranium-lead ages. Geochim. Cosmochim. Acta 62 (4):665–676.

Majaule, T.; Hanson, R. E.; Key, R. M.; Singletary, S. J.; Martin, M. W.; and Bowring, S. A. 2001. The Magondi Belt in northeast Botswana: regional relations and new geochronological data from the Sua Pan area. J. Afr. Earth Sci. 32:257–267.

Malusà, M. G.; Resentini, A.; and Garzanti, E. 2016. Hydraulic sorting and mineral fertility bias in detrital geochronology. Gondwana Res. 31:1–19.

Master, S.; Bekker, A.; and Hofmann, A. 2010. A review of the stratigraphy and geological setting of the Palaeoproterozoic Magondi Supergroup, Zimbabwe—type locality for the Lomagundi carbon isotope excursion. Precambrian Res. 182(4):254–273.

McCarthy, T. S.; Humphries, M. S.; Mahomed, I.; Le Roux, P.; and Verhagen, B. T. 2012. Island forming processes in the Okavango Delta, Botswana. Geomorphology 179:249–257.

McCarthy, T. S.; Smith, N. D.; Ellery, W. N.; and Gumbricht, T. 2002. The Okavango Delta—semiarid alluvial-fan sedimentation related to incipient rifting. *In* Renaut, R. E., and Ashley, G. M., eds. Sedimentation in continental rifts. SEPM Spec. Publ. 73:179–194.

McCourt, S.; Armstrong, R. A.; Jelsma, H.; and Mapeo, R. B. M. 2013. New U-Pb SHRIMP ages from the Lubango region, SW Angola: insights into the Palaeoproterozoic evolution of the Angolan Shield, southern Congo Craton, Africa. J. Geol. Soc. Lond. 170(2):353–363.

McFarlane, M. J.; Eckardt, F. D.; Coetzee, S. H.; and Ringrose, S. 2010. An African surface weathering profile in the Kalahari of North West Ngamiland, Botswana: processes and products. Z. Geomorphol. 54(3):273–303.

McKay, M. P.; Coble, M. A.; Hessler, A. M.; Weislogel, A. L.; and Fildani, A. 2016. Petrogenesis and provenance of distal volcanic tuffs from the Permian–Triassic Karoo Basin, South Africa: a window into a dissected magmatic province. Geosphere 12(1):1–14.

McLennan, S. M.; Hemming, S.; McDaniel, D. K.; and Hanson, G. N. 1993. Geochemical approaches to sedimentation, provenance, and tectonics. *In* Johnsson, M. J., and Basu, A. eds. Processes controlling the composition of clastic sediments. Geol. Soc. Am. Spec. Pap. 284:21–40.

Milliman, J. D., and Farnsworth, K. L. 2011. River discharge to the coastal ocean: a global synthesis. Cambridge, Cambridge University Press, 384 p.

Milliman, J. D., and Meade, R. H. 1983. World-wide delivery of river sediment to the oceans. J. Geol. 91(1):1–21.

Moore, A., and Blenkinsop, T. 2002. The role of mantle plumes in the development of continental-scale drainage patterns: the southern African example revisited. S. Afr. J. Geol. 105(4):353–360.

Moore, A. E.; Cotterill, F. P. D.; Broderick, T. G.; and Plowes, D. 2009. Landscape evolution in Zimbabwe from the Permian to present, with implications for kimberlite prospecting. S. Afr. J. Geol. 112(1):65–86.

Moore, A. E.; Cotterill, F. P. D.; and Eckardt, F. D. 2012. The evolution and ages of Makgadikgadi palaeo-lakes: consilient evidence from Kalahari drainage evolution south-central Africa. S. Afr. J. Geol. 115(3):385–413.

Moore, A. E.; Cotterill, F. P. D.; Main, M. P. L.; and Williams, H. B. 2007. The Zambezi River. *In* Gupta, A., ed. Large rivers: geomorphology and management. Chichester, Wiley, p. 311–332.

Moore, A. E., and Larkin, P. A., 2001. Drainage evolution in south-central Africa since the breakup of Gondwana. S. Afr. J. Geol. 104(1):47–68.

Moore, D. M., and Reynolds, R. C. 1997. X-ray diffraction and the identification and analysis of clay minerals (2nd ed.). Oxford, Oxford University Press.

Mzuza, M. K.; Zhang, W.; Kapute, F.; and Wei, X. 2019. The impact of land use and land cover changes on the Nkula Dam in the Middle Shire River catchment, Malawi. *In* Pepe, A., and Zhao, Q., eds. Geospatial analyses of earth observation (EO) data. London, IntechOpen, p. 37–66.

Nesbitt, H. W., and Young, G. M. 1982. Early Proterozoic climates and plate motions inferred from major element chemistry of lutites. Nature 299:715–717.

Nugent, C. 1990. The Zambezi River: tectonism, climatic change, and drainage evolution. Palaeogeogr. Palaeoclimatol. Palaeoecol. 78:55–69.

Nyambe, I. A. 1999. Tectonic and climatic controls on sedimentation during deposition of the Sinakumbe Group and Karoo Supergroup, in the mid-Zambezi Valley Basin, southern Zambia. J. Afr. Earth Sci. 28(2):443–463.

Odom, I. E.; Doe, T. W.; and Dott, R. H. 1976. Nature of feldspar-grain size relations in some quartz-rich sandstones. J. Sediment. Petrol. 46(4):862–870.

Parker, A. 1970. An index of weathering for silicate rocks. Geol. Mag. 107:501–504.

Partridge, T. C., and Maud, R. R. 1987. Geomorphic evolution of southern Africa since the Mesozoic. S. Afr. J. Geol. 90(2):179–208.

Pastore, G.; Baird, T.; Vermeesch, P.; Bristow, C.; Resentini, A.; and Garzanti, E. 2021. Provenance and recycling of Sahara Desert sand. Earth-Sci. Rev. 216:103606. https://doi.org/10.1016/j.earscirev.2021.103606.

Ponte, J. P.; Robin, C.; Guillocheau, F.; Popescu, S.; Suc, J. P.; Dall'Asta, M.; Melinte-Dobrinescu, M. C.; Bubik, M.; Dupont, G.; and Gaillot, J. 2019. The Zambezi delta (Mozambique Channel, East Africa): high resolution dating combining bio-orbital and seismic stratigraphies to determine climate (palaeoprecipitation) and tectonic controls on a passive margin. Mar. Pet. Geol. 105:293–312.

Price, J. R., and Velbel, M. A. 2003. Chemical weathering indices applied to weathering profiles developed on heterogeneous felsic metamorphic parent rocks. Chem. Geol. 202(3–4):397–416.

Reason, C. J. C.; Landman, W.; and Tennant, W. 2006. Seasonal to decadal prediction of southern African climate and its links with variability of the Atlantic Ocean. Bull. Am. Meteorol. Soc. 87(7):941–955.

Resentini, A.; Andò, S.; Garzanti, E.; Malusà, M. G.; Pastore, G.; Vermeesch, P.; Chanvry, E.; and Dall'Asta, M. 2020. Zircon as a provenance tracer: coupling Raman spectroscopy and U-Pb geochronology in source-to-sink studies. Chem. Geol. 555:119828.

Resentini, A.; Goren, L.; Castelltort, S.; and Garzanti, E. 2017. Partitioning sediment flux by provenance and tracing erosion patterns in Taiwan. J. Geophys. Res. Earth Surf. 122(7):1430–1454.

Rieu, R.; Allen, P. A.; Plötze, M.; and Pettke, T. 2007. Climatic cycles during a Neoproterozoic "snowball" glacial epoch. Geology 35(4):299–302.

Ronco, P.; Fasolato, G.; Nones, M.; and Di Silvio, G. 2010. Morphological effects of damming on lower Zambezi River. Geomorphology 115(1–2):43–55.

Rubey, W. W. 1933. The size distribution of heavy minerals within a water-laid sandstone. J. Sediment. Petrol. 3(1):3–29.

Rudnick, R. L., and Gao, S. 2003. Composition of the continental crust. *In* Rudnick, R. L., ed. The crust. Vol. 3 of Treatise on geochemistry. Amsterdam, Elsevier, p. 1–64.

Schulz, H.; Lückge, A.; Emeis, K. C.; and Mackensen, A. 2011. Variability of Holocene to Late Pleistocene Zambezi riverine sedimentation at the upper continental slope off Mozambique, 15°–21°S. Mar. Geol. 286:21–34.

Setti, M.; López-Galindo, A.; Padoan, M.; and Garzanti, E. 2014. Clay mineralogy in southern Africa river muds. Clay Miner. 49:717–733.

Shaw, A. I. 2009. The characterisation of calcrete based on its environmental settings within selected regions of the Kalahari, southern Africa. PhD thesis, University of Oxford, 606 p.

Shaw, P., and Thomas, D. S. G. 1992. Geomorphology, sedimentation, and tectonics in the Kalahari Rift. Isr. J. Earth Sci. 41:87–94.

Siwedza, S.; Mukonzo, S.; Ngambi, C.; and Shava, S. 2021. Impacts of cyclones Idai and Kenneth and the 2019 floods on the insurance sector in South Africa and Mozambique. *In* Nhamo, G., and Chapungu, L., eds. The increasing risk of floods and tornadoes in southern Africa (Sustainable Development Goals Ser.). Cham, Springer, p. 157–171. https://doi.org/10.1007/978-3-030-74192-1_9.

Sláma, J.; Košler, J.; Condon, D. J.; Crowley, J. L.; Gerdes, A.; Hanchar, J. M.; Horstwood, M. S.; et al. 2008. Plešovice zircon—a new natural reference material for U-Pb and Hf isotopic microanalysis. Chem. Geol. 249:1–35.

Söderlund, U.; Hofmann, A.; Klausen, M. B.; Olsson, J. R.; Ernst, R. E.; and Persson, P. O. 2010. Towards a complete magmatic barcode for the Zimbabwe craton: baddeleyite U-Pb dating of regional dolerite dyke swarms and sill complexes. Precambrian Res. 183(3):388–398.

Svensen, H.; Corfu, F.; Polteau, S.; Hammer, Ø.; and Planke, S. 2012. Rapid magma emplacement in the Karoo Large Igneous Province. Earth Planet. Sci. Lett. 325–326:1–9.

Tanaka, T.; Togashi, S.; Kamioka, H.; Amakawa, H.; Kagami, H.; Hamamoto, T.; Yuhara, M.; et al. 2000. JNdi-1: a neodymium isotopic reference in consistency with La Jolla neodymium. Chem. Geol. 168(3–4):279–281.

Taylor, S. R., and McLennan, S. M. 1995. The geochemical evolution of the continental crust. Rev. Geophys. 33:241–265.

Thiéblemont, D.; Chêne, F.; Liégeois, J.-P.; Ouabadi, A.; Le Gall, B.; Maury, R. C.; Jalludin, M.; Ouattara

Gbélé, C.; Tchaméni, R.; and Fernandez-Alonso, M. 2016. Geological map of Africa at 1:10 million scale. Orléans, CGMW-BRGM (Commission for the Geological Map of the World–Bureau de Recherches Géologiques et Minières).

Thomas, D. S. G., and Shaw, P. A. 1988. Late Cainozoic drainage evolution in the Zambezi basin: evidence from the Kalahari rim. J. Afr. Earth Sci. 7:611–618.

———. 1991. The Kalahari environment. Cambridge, Cambridge University Press, 287 p.

Totten, M. W.; Hanan, M. A.; and Weaver, B. L. 2000. Beyond whole-rock geochemistry of shales: the importance of assessing mineralogic controls for revealing tectonic discriminants of multiple sediment sources for the Ouachita Mountain flysch deposits. Geol. Soc. Am. Bull. 112(7):1012–1022.

Vainer, S.; Matmon, A.; Erel, Y.; Hidy, A. J.; Crouvi, O.; De Wit, M.; Geller, Y.; and ASTER Team 2021. Landscape responses to intraplate deformation in the Kalahari constrained by sediment provenance and chronology in the Okavango Basin. Basin Res. 33 (2):1170–1193.

van der Lubbe, H. J. L.; Frank, M.; Tjallingii, R.; and Schneider, R. R. 2016. Neodymium isotope constraints on provenance, dispersal, and climate-driven supply of Zambezi sediments along the Mozambique Margin during the past ~45,000 years. Geochem. Geophys. Geosyst. 17(1):181–198.

van der Lubbe, J. (H.) J. L.; Tjallingii, R.; Prins, M. A.; Brummer, G.-J. A.; Jung, S. J. A.; Kroon, D.; and Schneider, R. R. 2014. Sedimentation patterns off the Zambezi River over the last 20,000 years. Mar. Geol. 355:189–201.

Van Loon, A. T., and Mange, M. A. 2007. "In situ" dissolution of heavy minerals through extreme weathering, and the application of the surviving assemblages and their dissolution characteristics to correlation of Dutch and German silver sands. In Mange, M. A., and Wright, D. T., eds. Heavy minerals in use (Dev. Sedimentol., vol. 58). Amsterdam, Elsevier, p. 189–213.

Velbel, M. A. 2007. Surface textures and dissolution processes of heavy minerals in the sedimentary cycle: examples from pyroxenes and amphiboles. In Mange, M. A., and Wright, D. T., eds. Heavy minerals in use (Dev. Sedimentol., vol. 58). Amsterdam, Elsevier, p. 113–150.

Velde, B. 1995. Origin and mineralogy of clays. Berlin, Springer.

Velde, B., and Meunier, A. 2008. The origin of clay minerals in soils and weathered rocks. Berlin, Springer, 405 p.

Vermeesch, P. 2012. On the visualisation of detrital age distributions. Chem. Geol. 312–313:190–194.

———. 2018. IsoplotR: a free and open toolbox for geochronology. Geosci. Front. 9:1479–1493.

———. 2021. On the treatment of discordant detrital zircon U-Pb data. Geochronology 3(1):247–257.

Vermeesch, P., and Garzanti, E., 2015. Making geological sense of 'Big Data' in sedimentary provenance analysis. Chem. Geol. 409:20–27.

Vermeesch, P.; Resentini, A.; and Garzanti, E. 2016. An R package for statistical provenance analysis. Sediment. Geol. 336:14–25.

Vermeesch, P.; Rittner, M.; Petrou, E.; Omma, J.; Mattinson, C.; and Garzanti, E. 2017. High throughput petrochronology and sedimentary provenance analysis by automated phase mapping and LAICPMS. Geochem. Geophys. Geosyst. 18:4096–4109.

Vezzoli, G.; Garzanti, E.; Limonta, M.; Andò, S.; and Yang, S. 2016. Erosion patterns in the Changjiang (Yangtze River) catchment revealed by bulk-sample versus single-mineral provenance budgets. Geomorphology 261:177–192.

von Eynatten, H.; Barcelò-Vidal, C.; and Pawlowsky-Glahn, V. 2003. Composition and discrimination of sandstones: a statistical evaluation of different analytical methods. J. Sediment. Res. 73(1):47–57.

von Eynatten, H.; Tolosana-Delgado, R.; and Karius, V. 2012. Sediment generation in modern glacial settings: grain-size and source-rock control on sediment composition. Sediment. Geol. 280:80–92.

von Eynatten, H.; Tolosana-Delgado, R.; Karius, V.; Bachmann, K.; and Caracciolo, L. 2016. Sediment generation in humid Mediterranean setting: grain-size and source-rock control on sediment geochemistry and mineralogy (Sila Massif, Calabria). Sediment. Geol. 336:68–80.

Vörösmarty, C. J., and Moore, B. M., III. 1991. Modeling basin-scale hydrology in support of physical climate and global biogeochemical studies: an example using the Zambezi River. Surv. Geophys. 12(1–3):271–311.

Walford, H. L.; White, N. J.; and Sydow, J. C. 2005. Solid sediment load history of the Zambezi Delta. Earth Planet. Sci. Lett. 238(1–2):49–63.

Wellington, J. 1955. Southern Africa: a geographical study. Vol. 1. Physical geography, climate, vegetation, and soils: hydrography. Cambridge, Cambridge University Press, 528 p.

Weltje, G. J. 1997. End-member modeling of compositional data: numerical-statistical algorithms for solving the explicit mixing problem. Math. Geol. 29(4):503–549.

Westerhof, A. P.; Lehtonen, M. I.; Mäkitie, H.; Manninen, T.; Pekkala, Y.; Gustafsson, B.; and Tahon, A. 2008. The Tete-Chipata Belt: a new multiple terrane element from western Mozambique and southern Zambia. In Pekkala, Y.; Lehto, T.; and Mäkitie, H., eds. GTK Consortium geological surveys in Mozambique 2002–2007. Geol. Surv. Finl. Spec. Pap. 48:145–166.

Wilson, M. J. 1999. The origin and formation of clay minerals in soils: past, present and future perspectives. Clay Miner. 34(1):7–25.

Wittmann, H.; Oelze, M.; Gaillardet, J.; Garzanti, E.; and von Blanckenburg, F. 2020. A global rate of denudation from cosmogenic nuclides in the Earth's largest rivers. Earth-Sci. Rev. 204:103147.

REFERENCES CITED ONLY IN THE APPENDIX

Andò, S.; Morton, A.; and Garzanti, E. 2014. Metamorphic grade of source rocks revealed by chemical fingerprints of detrital amphibole and garnet. *In* Scott, R.; Smyth, H.; Morton, A.; and Richardson, N., eds. Sediment provenance studies in hydrocarbon exploration and production. Geol. Soc. Lond. Spec. Publ. 386:351–371.

Fedo, C. M.; Nesbitt, H. W.; and Young, G. M. 1995. Unraveling the effects of potassium metasomatism in sedimentary rocks and paleosols, with implications for paleoweathering conditions and provenance. Geology 23:921–924.

Garzanti, E. 2019. Petrographic classification of sand and sandstone. Earth-Sci. Rev. 192:545–563.

Garzanti, E., and Vezzoli, G. 2003. A classification of metamorphic grains in sands based on their composition and grade. J. Sediment. Res. 73:830–837.

Garzanti, E.; Vezzoli, G.; Andò, S.; Lavé, J.; Attal, M.; France-Lanord, C.; and DeCelles, P. 2007. Quantifying sand provenance and erosion (Marsyandi River, Nepal Himalaya). Earth Planet. Sci. Lett. 258(3–4):500–515.

Garzanti, E.; Vezzoli, G.; Andò, S.; Paparella, P.; and Clift, P. D. 2005. Petrology of Indus River sands: a key to interpret erosion history of the Western Himalayan Syntaxis. Earth Planet. Sci. Lett. 229(3–4):287–302.

Haley, B. A.; Klinkhammer, G. P.; and McManus, J. 2004. Rare earth elements in pore waters of marine sediments. Geochim. Cosmochim. Acta 68:1265–1279.

Harnois, L. 1988. The CIW index: a new chemical index of weathering. Sediment. Geol. 55:319–322.

Hubert, J. F. 1962. A zircon-tourmaline-rutile maturity index and the interdependence of the composition of heavy minerals assemblages with the gross composition and texture of sandstones. J. Sediment. Petrol. 32:440–450.

Moore, D. M., and Reynolds, R. C. 1989. X-ray diffraction and the identification and analysis of clay minerals. Oxford, Oxford University Press.